

Diss ETH Nr. 12161

# **Brillouin-spectroscopy on thin films and intermediate valent rare earth compounds**

Abhandlung zur Erlangung des Titels  
Doktor der Naturwissenschaften  
der Eidgenössischen Technischen Hochschule Zürich

vorgelegt von

**Urs Schärer**

Dipl. Phys. ETH

geboren am 15. Februar 1967

Bürger der Stadt Zürich

Angenommen auf Antrag von

Prof. Dr. P. Wachter, Zürich, Referent

Prof. Dr. G. Güntherodt, Aachen, Korreferent

1997

*meinen Eltern*

# Table of Contents

<b>Abstract</b> .....	<b>1</b>
<b>Kurzfassung</b> .....	<b>3</b>
<b>1 Introduction</b> .....	<b>5</b>
<b>2 Surface acoustic waves</b> .....	<b>9</b>
2.1 Strain, stress, and elastic constants .....	9
2.1.1 Strain .....	10
2.1.2 Stress .....	10
2.1.3 Hook's Law .....	10
2.1.4 Symmetry of the elastic and compliance tensors .....	12
2.2 Elastical properties of cubic crystals .....	14
2.2.1 Bulk modulus .....	14
2.2.2 Poisson's ratio .....	16
2.2.3 Anisotropy .....	17
2.3 Wave equation .....	18
2.4 Bulkwaves .....	18
2.5 SAW in a semi infinite material .....	20
2.5.1 Rayleigh type solution .....	20
2.5.2 Angular Dispersion of an anisotropic cubic medium .....	23
2.5.3 Amplitude of a SAW .....	28
2.6 SAW in a thin film .....	29
2.6.1 Angular dispersion .....	31
2.6.2 $qd$ -dispersion .....	31
2.7 SAW in a multi-film-system .....	33
2.7.1 Superlattice on a substrate .....	34
<b>3 Brillouin spectroscopy</b> .....	<b>35</b>
3.1 Inelastic light scattering on acoustic phonons .....	36
3.2 Cross section on surface acoustic waves .....	38
3.2.1 Mechanism of scattering .....	38
3.2.2 Polarization and incident angle of the light .....	39
3.2.3 Thermal influence .....	41
3.2.4 Conclusions .....	41
<b>4 Experimental details</b> .....	<b>43</b>
4.1 3+3-pass Fabry-Pérot interferometer .....	44
4.1.1 Principle of a Fabry-Pérot .....	44
4.1.2 Multipass Fabry-Pérot interferometer .....	46
4.2 Experimental Setup .....	50

---

<b>5 Thin film structures</b> .....	<b>53</b>
5.1 PbSe-layer on Si(111).....	53
5.1.1 Sample .....	54
5.1.2 Experimental details .....	55
5.1.3 Calculation of the elastic constants.....	56
5.1.4 Conclusions.....	56
5.2 CoSi <sub>2</sub> -films on Si(111) .....	57
5.2.1 Samples .....	58
5.2.2 Experimental details .....	59
5.2.3 Calculation of the elastic constants.....	61
5.2.4 Conclusions.....	62
5.3 CoSi <sub>2</sub> /Fe superlattices on Si(111).....	65
5.3.1 Samples .....	65
5.3.2 Experimental details .....	66
5.3.3 Calculation of the elastic constants.....	67
5.3.4 Conclusions.....	69
<b>6 Elastic properties of doped SmS</b> .....	<b>71</b>
6.1 Introduction .....	71
6.2 La doped SmS .....	74
6.2.1 Samples .....	75
6.2.2 Experimental details .....	77
6.2.3 Calculation of the elastic constants.....	77
6.2.4 Calculation of the valence .....	80
6.3 Tm doped SmS .....	83
6.3.1 Samples .....	84
6.3.2 Experimental details .....	86
6.3.3 Calculated elastic constants .....	86
6.4 Conclusions .....	89
<b>A Further elastic properties</b> .....	<b>91</b>
A.1 Elastic constants of polycrystalline materials .....	91
A.2 Lattice constant and Poisson's ratio in films.....	92
<b>B Numerical calculations of the SAW velocity</b> .....	<b>93</b>
<b>References</b> .....	<b>97</b>
<b>Publications</b> .....	<b>103</b>
<b>Presentations</b> .....	<b>105</b>
<b>Dank</b> .....	<b>107</b>
<b>Curriculum Vitae</b> .....	<b>109</b>

# List of Figures

2.1	Stress tensor .....	9
2.2	Stress-strain relation .....	11
2.3	Bulk modulus .....	15
2.4	Poisson's ratio .....	16
2.5	Propagation along [110] .....	17
2.6	Surface acoustic wave .....	20
2.7	Coordinate system for the surface wave system .....	21
2.8	Angular dispersion in a (001) plane of copper .....	24
2.9	Angular dispersion in a (001) plane of PbS .....	24
2.10	Angle between sagittal plane and displacement ellipse .....	25
2.11	Displacement angle in (001) plane of copper .....	25
2.12	Angular dispersion in a (011) plane of copper .....	26
2.13	Angular dispersion in a (001) plane of PbS .....	27
2.14	Angular dispersion in a (111) plane of copper .....	28
2.15	Amplitude of a SAW .....	29
2.16	SAW in thin film with underlying substrate .....	30
2.17	$qd$ -dispersion in a thin Fe film on a Si substrate along [100] .....	32
2.18	SAW in a multilayer system .....	33
3.1	Stokes and anti-Stokes process .....	35
3.2	Typical Brillouin spectrum .....	37
3.3	Scattering on surface ripples .....	39
3.4	Cross section depending on polarisation and incident angle .....	40
4.1	Principle of a Fabry-Pérot .....	43
4.2	Transmission function of a Fabry-Pérot .....	45
4.3	Transmission function of a tandem constellation .....	47
4.4	Principle of a 3+3 pass tandem Fabry-Pérot interferometer .....	49
4.5	Experimental setup .....	50
4.6	Sample holder .....	51
5.1	Angular dispersion of PbSe on Si(111) .....	55

---

5.2	CaF <sub>2</sub> and defect CsCl structure of CoSi <sub>2</sub> .....	57
5.3	Angular dispersion of CoSi <sub>2</sub> .....	59
5.4	Spectrum of CoSi <sub>2</sub> (Defect CsCl structure) .....	60
5.5	<i>qd</i> -dispersion of CoSi <sub>2</sub> .....	61
5.6	<i>qd</i> -dispersion of the CoSi <sub>2</sub> /Fe superlattice .....	67
5.7	Angular dispersion of CoSi <sub>2</sub> /Fe superlattice .....	68
6.1	Structure of doped SmS .....	71
6.2	Electronic band structure of doped SmS .....	73
6.3	Spectrum of Sm <sub>0.75</sub> La <sub>0.25</sub> S .....	76
6.4	Angular dispersion of La doped SmS .....	78
6.5	Elastic constants of La doped SmS .....	79
6.6	Poisson's ratio of La doped SmS .....	79
6.7	Valence and lattice constants of La doped SmS.....	81
6.8	Lattice constants and valence of Tm doped SmS .....	83
6.9	Spectra of Sm <sub>0.85</sub> Tm <sub>0.15</sub> S .....	85
6.10	Angular dispersion of Tm doped SmS .....	87
6.11	Elastic constants of Tm doped SmS .....	88
6.12	Poisson's ratio of Tm doped SmS .....	88
B.1	Determinant of the BC matrix versus the velocity .....	94

# List of Tables

2.1	Abbreviated subscript notation .....	12
4.1	Properties of several Fabry-Pérot interferometers .....	45
5.1	Properties of PbX ( $X = S, Se, Te$ ) .....	54
5.2	Elastic constants, Poisson's ratio and anisotropy of PbX .....	56
5.3	Lattice constant, density and Poisson's ratio of $CoSi_2$ .....	58
5.4	Elastic constants of $CoSi_2$ .....	63
5.5	Further elastic properties for $CoSi_2$ .....	63
5.6	Properties of $CoSi_2/Fe$ superlattices .....	65
5.7	Elastic constants of $CoSi_2/Fe$ superlattices .....	68
6.1	Lattice constants and densities of La doped SmS .....	75
6.2	Elastic constants, bulk moduli and Poisson's ratios of La doped SmS ...	80
6.3	Lattice constants and densities of Tm doped SmS .....	85
6.4	Elastic constants, bulk moduli and Poisson's ratios of Tm doped SmS .....	89

# Abstract

Inelastically scattered light of a laser was used to determine the velocity of *surface acoustic waves* (SAW) in metallic thin film structures and doped, intermediate valent SmS compounds. Generally, the light scattering on acoustic phonons is called *Brillouin spectroscopy*.

Surface acoustic waves are a superposition of plane, acoustic waves, which propagate along a surface plane and are exponentially damped perpendicular to it. In single crystals the velocity depends on the orientation of the plane and the direction of propagation. The determination of the SAW velocities in different directions gives the so called *angular dispersion*. In thin film structures there is additionally also a dependence on the product of the wave vector parallel to the surface ( $q$ ) and the thickness of the film ( $d$ ). The measurement of the velocity depending on  $qd$  is called *qd-dispersion*. From both sorts of dispersion all elastic constants of a sample (for a cubic symmetry  $C_{11}$ ,  $C_{12}$  and  $C_{44}$ ) can be calculated using an appropriate model function.

For thin film structures it is possible to get information about the quality of the layers. All films described in this work were grown on a (111) oriented silicon substrate. The elastic constants of the following samples have been determined:

- 3.5  $\mu\text{m}$  thick PbSe film. We found a drastic difference in the elastic constants of the thin PbSe-film and of a single crystal of PbSe.
- $\text{CoSi}_2$  films with two different crystallographic structures, one was a  $\text{CaF}_2$  and the other a defect CsCl structure. While the well known  $\text{CaF}_2$  phase was elastically anisotropic, the new defect CsCl phase behaved isotropically.
- $\text{CoSi}_2/\text{Fe}$  superlattice. The elastic constants of these structures depend strongly on the exact parameters of the layer system.

The elastic constants of intermediate valent single crystals allow to conclude on the electronic structure of the samples. One evidence of intermediate valence is a negative value of Poisson's ratio, which means that the crystal is extraordinarily



## Abstract

---

instable and that its volume collapses already, when an uniaxial pressure is applied. We measured doped SmS compounds, in which some of the Sm ions have been substituted by La or Tm ions. We found a clear connection between the doping concentration, the intermediate valence and the elastic behavior of the samples.

# Kurzfassung

Inelastisch gestreutes Licht eines Lasers wurde benutzt, um die Geschwindigkeit von *Oberflächenschallwellen* in metallischen Dünnschicht-Strukturen und dotierten zwischenvalenten SmS-Verbindungen zu bestimmen. Die Lichtstreuung an akustischen Phononen wird *Brillouin-Streuung* genannt.

Oberflächenschallwellen sind eine Superposition von ebenen, akustischen Wellen, welche an einer Oberfläche entlanglaufen und senkrecht dazu exponentiell gedämpft sind. In Einkristallen ist die Geschwindigkeit der Oberflächenschallwellen abhängig von der Orientierung der Oberfläche und der Ausbreitungsrichtung. Werden die Schallgeschwindigkeiten in verschiedenen Richtungen bestimmt, nennt man das die *Winkeldispersion*. In Dünnschicht-Strukturen kommt noch eine Abhängigkeit vom Produkt des Wellenvektors parallel zur Oberfläche ( $q$ ) und der Schichtdicke ( $d$ ) dazu. Die Messungen der Geschwindigkeit in Abhängigkeit von diesem Produkt  $qd$  nennt man *qd-Dispersion*.

Aus beiden Dispersionsarten können mit einem geeigneten Modell alle elastischen Konstanten einer Probe (im kubischen Fall  $C_{11}$ ,  $C_{12}$  und  $C_{44}$ ) berechnet werden. In den Dünnschicht-Strukturen können damit Aussagen über die Qualität der Schichten gemacht werden. Alle in dieser Arbeit untersuchten Schichten wurden epitaktisch auf (111)-orientiertes Silizium gewachsen. An folgenden Schichten wurden die elastischen Konstanten bestimmt:

- 3.5  $\mu\text{m}$  dicke PbSe-Schicht. Hier zeigte sich ein drastischer Unterschied in den elastischen Konstanten der Schichtstruktur und eines Einkristalls.
- $\text{CoSi}_2$  Schichten in zwei verschiedenen strukturellen Formen,  $\text{CaF}_2$  and  $\text{CsCl}$  mit Defekten. Während die Schichten der bekannter  $\text{CaF}_2$ -Form elastisch anisotrop waren, zeigten die Proben der neuen defekten  $\text{CsCl}$ -Phase ein isotropes Verhalten.
- $\text{CoSi}_2/\text{Fe}$  Supergitter. Die elastischen Konstanten dieser Proben hängen sehr stark von den exakten Schichtparametern ab.

In zwischervalenten Einkristallen können von den elastischen Konstanten Schlüsse auf die elektronische Struktur der Proben gezogen werden. Ein Beweis für Zwischenvalenz ist ein negatives Poisson Verhältnis, das besagt, dass der Kristall ausserordentlich weich ist und dass dessen Volumen schon bei einem uniaxial angelegten Druck in allen Richtungen kollabiert. Wir haben SmS Verbindungen untersucht, bei denen ein Teil der Sm-Ionen durch La- oder Tm-Ionen ersetzt wurde. Wir konnten einen klaren Zusammenhang zwischen der Stärke der Dotierung, der Zwischenvalenz und dem elastischen Verhalten aufzeigen.

# Chapter 1

## Introduction

In modern solid state physics the characterization of new materials by its elastic constants is important. The elastic behavior can give, e.g., information about the quality of samples (thin film structures) or the electronic structure (intermediate valence). One instrument to investigate the elastic properties of a material is the ultrasonic technique. This is a very powerful and precise tool, but as soon as the samples are quite small or only very thin it gets to its limits.

Another very elegant way, in a lot of aspects, is the use of Brillouin spectroscopy to determine the elastic constants. Because of the very small laser spot (when focused about  $\phi \approx 20 \mu\text{m}$ ) no large samples were needed. Samples of the size of 0.5 mm or less can still be investigated. Moreover, because of the lack of any mechanical contact to the crystal, the Brillouin spectroscopy method can be used under a lot of different conditions, e.g. the sample can be held in an inert atmosphere or in a cryostat.

For Brillouin spectroscopy the monochromatic light of a laser is scattered inelastically on acoustic phonons. Thereby the scattering shifts the energy or, respectively, the frequency of the incident photon a little. This very small energy shift (small only in the case of scattering on acoustic phonons) is detected and measured with a Fabry-Pérot-interferometer. Since the scattering vector is very small compared to the Brillouin zone, the dispersion relation of the acoustic mode is still in the linear range and the velocity of the surface acoustic wave can be easily calculated.

Depending on the optical quality of the samples, different sorts of acoustic waves can be observed: On transparent materials, where the absorption is only small, the normal *bulk waves* are detectable, but in metallic samples with their high reflectivity,

this mode can not be measured, because of the only very small penetration depth of light. Here the cross section for scattering on *surface acoustic waves* (SAW) becomes more important. Generally surface acoustic waves are a superposition of plane waves, which propagate along a surface and are exponentially damped perpendicular to the surface. Thereby the scattering process is located just at the surface and occurs from so called surface ripples. Nevertheless the penetration depth of a surface acoustic wave is several micrometers deep and, despite its surface character, the SAW probes the bulk of a sample in a good manner.

The measurement of the bulk wave velocities in the direction of a main symmetry axis allows very simply the calculation of the elastic constants of the crystal. On the other hand, due to the more complex nature of surface acoustic waves, the calculation of the elastic constants from the measured velocity of a surface acoustic wave is much more complicated, but nevertheless doable. E.g. in a crystal with a cubic symmetry there are three independent elastic constants ( $C_{11}$ ,  $C_{12}$  and  $C_{44}$ ). For the calculation either the dependence of the SAW velocity on the propagation direction of the wave in the surface plane (angular dispersion) or, alternatively – in the case of a thin film structure on a substrate –, the dependence on the product  $qd$  is used to fit the elastic constants ( $qd$ -dispersion).  $q$  stands for the wave vector parallel to the surface and  $d$  for the thickness of the film.

In this work, we show, how the surface acoustic waves can be used to determine the elastic constants of single crystals and thin film structures.

First, in chapter 2, the definitions of stress, strain and the tensors of the elastic stiffness and the elastic compliance constants will be introduced. Then, after the introduction of the elastic wave equation and bulk waves, the most simple solution of the wave equation, the nature of the surface acoustic waves will be explained and their behavior will be analyzed in detail for a SAW in a semi-infinite body and in thin film structures on a substrate.

Chapter 3 will describe the scattering mechanism on acoustic waves. After the introduction of the Stokes and the anti-Stokes process, the calculation of the phonon velocity from a measured energy shift will be derived. Furthermore, the differences

---

of the scattering mechanism on a bulk wave and on a surface acoustic wave will be discussed. Finally, the cross section for scattering on surface acoustic waves will be given depending on the polarization of the incident and scattered photon and on the angle of the incident laser beam.

In chapter 4 the principle of the used Sandercock 3+3 pass tandem Fabry-Pérot interferometer will be explained. In the second part the experimental setup and its parameters will be presented.

Chapter 5 will deal with the elastic constants of thin film structures. These structure were all grown by molecular beam epitaxy on a (111) oriented silicon substrate. Three different materials were examined:

- A PbSe film on silicon, where the elastic constants of the film are compared with the elastic constants of a PbSe single crystal. The PbSe film was quite thick ( $3.5 \mu\text{m}$ ) and relaxed, but the remaining strain, induced by the different lattice constant of the silicon substrate, changes the elastic constants drastically.
- $\text{CoSi}_2$  films with two different crystallographic structures, the well known  $\text{CaF}_2$  structure and the new defect CsCl structure. Opposite to the results of the  $\text{CaF}_2$  structure, the experiments and the calculation on the defect CsCl structure show, that this form of  $\text{CoSi}_2$  behaves elastically isotropic and its structure can be interpreted as an average of a polycrystalline, randomly oriented  $\text{CaF}_2$  structure, despite its well defined single crystalline form. The silicon atoms of the  $\text{CoSi}_2$  film have only a very small influence on the elastic behavior.
- On  $\text{CoSi}_2/\text{Fe}$  superlattices the measurements show, that the elastic constants depend strongly on the exact parameters of the single layers in the superlattice (thickness of the  $\text{CoSi}_2$  and the Fe layer, number of periods).

In chapter 6 the elastic constants of doped SmS crystals will be presented and discussed. Under pressure SmS makes a semiconductor-metal transition. After this transition SmS is in an intermediate valent state. SmS can also be brought into this state without any applied pressure by substituting Sm by Y, La or Tm.

A strong evidence of intermediate valence is a negative  $C_{12}$  and a negative

value of Poisson's ratio, which can be calculated from the elastic constants. The presented data will show, that depending on the doping concentration  $\text{Sm}_{1-x}\text{La}_x\text{S}$  and  $\text{Sm}_{1-x}\text{Tm}_x\text{S}$  have both a more or less negative Poisson's ratio and are therefore in the intermediate valent state.

We will show, that the mechanism leading to intermediate valence is different for doping with La or Tm, due to the very different ionic radii. Since the Tm ion is clearly smaller than the Sm ion, the substitution sets the SmS crystal under an internal chemical pressure. On the other hand, La with its only minutely smaller ionic radius can hardly set the crystal under an adequate pressure. Here the intermediate valent behavior must be only the effect of the additional free electrons in the  $5d$  band, induced by building in trivalent La-atoms.

# Chapter 2

## Surface acoustic waves

To understand the theory of surface acoustic waves, the nature of vibration in a solid body has to be analyzed first. For this consideration the atomic nature can be neglected and the sample can be assumed as a continuum. The material properties, which describe the quality of an acoustic wave, are the density  $\rho$  and the elastic tensor  $c_{ijkl}$ .

### 2.1 Strain, stress, and elastic constants

In this section we will define the strain, the stress and the tensors of the elastic stiffness and the compliance. Furthermore the widely used abbreviated notation is introduced.

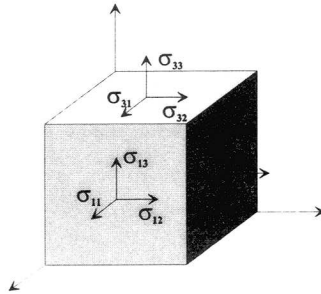


Fig. 2.1  $\sigma_{ij}$  represents the stress on the  $i$ -plane in the  $j$ -direction



### 2.1.1 Strain

The deformation of a solid body and therefore the movement of an infinitesimal small particle can be described by the strain  $\varepsilon_{ij}$ . The strain is defined as the differential displacement of the particle out of its equilibrium position [1]:

$$\varepsilon_{ij} = \frac{1}{2} \left[ \frac{\partial u_i}{\partial x_j} + \frac{\partial u_j}{\partial x_i} \right] \quad i, j = 1, 2, 3 \quad 2.1$$

where  $u_i$  is the displacement vector of the particle. Obviously  $\varepsilon_{ij}$  is a symmetric  $3 \times 3$ -matrix.

### 2.1.2 Stress

When a particle is moved out of its equilibrium position, elastic restoring forces develop between neighboring particles. These forces can be described by internal traction forces and stresses which act on the surface of a particle [1, 2]. They are represented by the stress tensor  $\sigma_{ij}$ , which is a symmetric  $3 \times 3$ -matrix as well. The diagonal terms  $\sigma_{ii}$  represent the stresses in the  $i$ -direction on the  $i$ -plane, while the off-diagonal terms  $\sigma_{ij}$  ( $i \neq j$ ) describe the traction forces on the  $i$ -plane in the  $j$ -direction (Fig. 2.1).

### 2.1.3 Hook's Law

Obviously any applied stress  $\sigma_{ij}$  produces a certain strain  $\varepsilon_{kl}$  and vice versa. Generally this can be written as:

$$\varepsilon_{kl} = f(\sigma_{ij}) \quad \text{and} \quad \sigma_{ij} = g(\varepsilon_{kl}) \quad g \equiv f^{-1} \quad 2.2$$

As long as the deformations are small the stress increases linearly with the strain. With increasing deformation the relation between the stress and the strain becomes

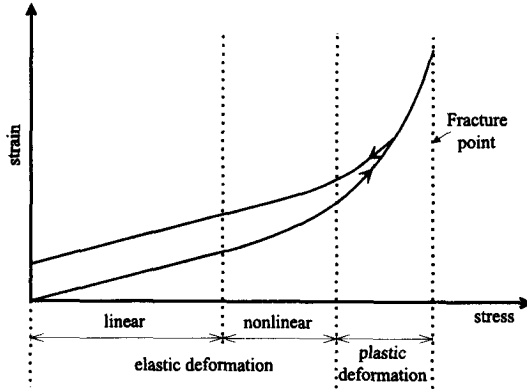


Fig. 2.2 typical stress-strain relation for a solid body [1]

more and more nonlinear, but still remains reversible. These regions are called linear and nonlinear *elastic deformation* (Fig. 2.2). If the stress increases beyond the elastic limit, which lies for the strain typically in the range of  $10^{-4}$  to  $10^{-3}$ , the solid deforms plastically and permanently. At last it fractures.

For this study we assume to be always in the range of the linear elastic deformations. Then, Eq. 2.2 can be written in a linear form called *Hook's Law* [1]<sup>1</sup>:

$$\sigma_{ij} = c_{ijkl} \cdot \epsilon_{kl} \quad 2.3$$

$$\epsilon_{kl} = s_{ijkl} \cdot \sigma_{ij} \quad 2.4$$

The linear operator in Eq. 2.3,  $c_{ijkl}$ , is called *elastic stiffness constants* or simply *elastic constants*, whereas  $s_{ijkl}$  in Eq. 2.4 is called *compliance constants*. Both,  $c_{ijkl}$  and  $s_{ijkl}$ , are tensors of 4<sup>th</sup> rank with totally 81 elements and, of course,  $c_{ijkl} \equiv (s_{ijkl})^{-1}$ .

<sup>1</sup> In this work Einstein's convention of summing over repeated subscripts is used. E.g. Eq. 2.3 is equivalent to

$$\sigma_{ij} = \sum_{k=1}^3 \sum_{l=1}^3 c_{ijkl} \cdot \epsilon_{kl}$$

$ij, kl$	11	22	33	12, 21	13, 31	23, 32
$I, J$	1	2	3	4	5	6

**Table 2.1** The double subscripts  $ij$  and  $kl$  are replaced by the single subscripts  $I$  and  $J$

### 2.1.4 Symmetry of the elastic and compliance tensors

With its 81 elements the stiffness and the compliance tensors are quite difficult to handle. But fortunately not all elements are independent. Using symmetry arguments the number of independent elements can be reduced rapidly.

#### Simple symmetries of Hook's Law:

From the symmetry of the stress tensor ( $\sigma_{ij} = \sigma_{ji}$ ) and from Eq. 2.3 the symmetry  $c_{ijkl} = c_{jikl}$  follows immediately [1, 3]. Similarly the symmetry of the strain tensor leads to  $c_{ijkl} = c_{ijlk}$ . Therefore the independent elements are reduced down to 36. The same can be done with the compliance tensor  $s_{ijkl}$ .

#### Abbreviated subscripts notation:

In the literature an other notation is often used for  $\sigma_{ij}$ ,  $\varepsilon_{kl}$ ,  $c_{ijkl}$  and  $s_{ijkl}$ . There the symmetry is used to write the  $3 \times 3$ -matrix of the stress and the strain as a 6-dimensional vector. Then, the 4<sup>th</sup>-rank tensor of the elastic and the compliance constants is expressed by a  $6 \times 6$ -matrix. To do so abbreviated subscripts are introduced. Therefore, one pair of a double index ( $ij$  or  $kl$ ) is replaced by a single subscript ( $I$  or  $J$ ) [4], following the convention depicted in Table 2.1. Then  $\sigma_{ij}$ ,  $\varepsilon_{kl}$ ,  $c_{ijkl}$  and  $s_{ijkl}$  transform according to [1]:

$$\begin{aligned}
 \sigma_I &= \sigma_{ij} && \text{for } I = 1 \dots 6 \\
 \varepsilon_I &= \begin{cases} \varepsilon_{ij} & \text{for } I = 1, 2, 3 \\ 2 \cdot \varepsilon_{ij} & \text{for } I = 4, 5, 6 \end{cases} \\
 C_{IJ} &= c_{ijkl} && \text{for } I, J = 1 \dots 6 \\
 S_{IJ} &= s_{ijkl} && \text{for } I, J = 1 \dots 6
 \end{aligned} \tag{2.5}$$

Hook's Law (Eq. 2.3 and Eq. 2.4) can then be simply written as:

$$\sigma_I = C_{IJ} \cdot \varepsilon_J \quad 2.6$$

$$\varepsilon_I = S_{IJ} \cdot \sigma_J$$

Although the tensors with the abbreviated subscripts look like ordinary tensors, one has to be very careful when transforming the base (e.g. rotating the coordinate-system). This has to be done in the normal tensor notation. The law of transformation is then for the stress and the strain [3]:

$$\sigma'_{ij} = a_{ik} \cdot a_{jl} \cdot \sigma_{kl} \quad 2.7$$

$$\varepsilon'_{ij} = a_{ik} \cdot a_{jl} \cdot \varepsilon_{kl} \quad 2.8$$

and for the elastic stiffness constants and the compliance constants:

$$c'_{ijkl} = a_{im} \cdot a_{jn} \cdot a_{ko} \cdot a_{lp} \cdot c_{mnop} \quad 2.9$$

$$s'_{ijkl} = a_{im} \cdot a_{jn} \cdot a_{ko} \cdot a_{lp} \cdot s_{mnop} \quad 2.10$$

where  $a_{ij}$  is the *orthogonal*  $3 \times 3$ -transformation matrix.

### Symmetry of the energy density:

Using the strain energy density, which is defined according to [2] as:

$$u\varepsilon = \frac{1}{2} \varepsilon_I \cdot C_{IJ} \cdot \varepsilon_J \quad 2.11$$

the symmetry of the elastic tensor matrix ( $C_{IJ} = C_{JI}$ ) can be easily verified. Thus, the number of the independent elastic constants can be reduced from 36 down to 21.  $C_{JL}$  finally looks like:

$$\begin{bmatrix} C_{11} & C_{12} & C_{13} & C_{14} & C_{15} & C_{16} \\ C_{12} & C_{22} & C_{23} & C_{24} & C_{25} & C_{26} \\ C_{13} & C_{23} & C_{33} & C_{34} & C_{35} & C_{36} \\ C_{14} & C_{24} & C_{34} & C_{44} & C_{45} & C_{46} \\ C_{15} & C_{25} & C_{35} & C_{45} & C_{55} & C_{56} \\ C_{16} & C_{26} & C_{36} & C_{46} & C_{56} & C_{66} \end{bmatrix} \quad 2.12$$

**Crystal symmetry:**

It is not possible to obtain further symmetries alone from the laws of the elasticity. However, the crystal symmetry, which is given by its atomic structure, can effectively simplify the tensor of the elastic constants. E.g. a crystal with a cubic symmetry has only 3 independent terms unequal zero [1–3]:

$$\begin{bmatrix} C_{11} & C_{12} & C_{12} & & & \\ C_{12} & C_{11} & C_{12} & & & \\ C_{12} & C_{12} & C_{11} & & & \\ & & & C_{44} & & \\ & & & & C_{44} & \\ & & & & & C_{44} \end{bmatrix} \quad 2.13$$

all other terms are equal zero. If the crystal is furthermore elastically isotropic – no crystal direction can elastically be distinguished –,  $C_{44}$  can be replaced by the term  $\frac{1}{2}(C_{11} - C_{12})$ .  $C_{IJ}$  and its inverse, the compliance tensor, have always the same number of independent elements.

## 2.2 Elastical properties of cubic crystals

In an experiment rarely the elastic constants  $C_{IJ}$  can be measured directly. Often only a function of  $C_{IJ}$  is observed. Consequently, the following observables, which describe the behavior of the solid body under certain circumstances, are defined in the literature :

### 2.2.1 Bulk modulus

When a hydrostatic pressure is applied to a crystal, the isotherm compressibility  $\kappa$  describes the relative behavior of the volume (Fig. 2.3). The bulk modulus  $B$  is

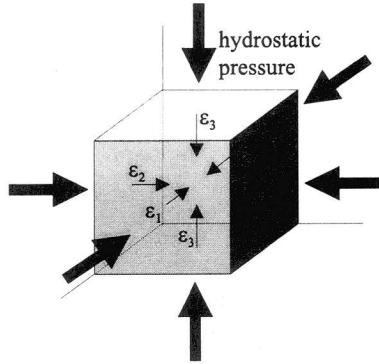


**Fig. 2.3** A hydrostatic pressure changes the volume of a material. Within the elastic limit the bulk modulus is the proportionality factor between the applied pressure and the volume change.

the reciprocal of  $\kappa$  and both are defined by the thermodynamical expression:

$$\frac{1}{B} = \kappa = - \left. \frac{1}{V} \frac{\partial V}{\partial p} \right|_T \quad 2.14$$

For a cubic crystal, where in all directions the strain  $\varepsilon_J$  is equal ( $= \varepsilon$ ), the bulk modulus can be expressed by  $C_{IJ}$ , using the following identities:

$$\begin{aligned} \partial p &= dp_I = C_{IJ} \cdot \varepsilon_J = \varepsilon \cdot (C_{11} + 2C_{12}) \\ \partial V &= dV = V \cdot (1 - \varepsilon)^3 - V \approx -3V \cdot \varepsilon \end{aligned}$$

Then Eq. 2.14 becomes [2]

$$B = \frac{1}{\kappa} = \frac{1}{3} \cdot (C_{11} + 2C_{12}) \quad 2.15$$

The harder the material is, the bigger the bulk modulus becomes. Typical values for  $B$  are several 10 GPa.

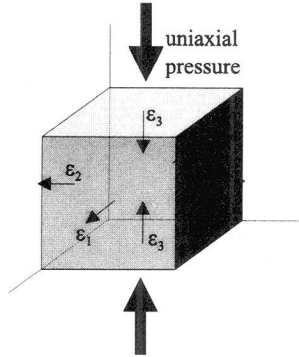


**Fig. 2.4** *An uniaxial pressure produces a negative strain ( $\epsilon_3$ ) parallel and a positive or negative strain ( $\epsilon_1$  and  $\epsilon_2$ ) perpendicular to the pressure. The ratio of the strains defines Poisson's ratio.*

## 2.2.2 Poisson's ratio

When an uniaxial pressure is applied to a crystal, Poisson's ratio  $\nu$  describes the ratio between the strain parallel and perpendicular to the direction of pressure [1]. For a cubic material it can be defined only along a crystallographic main axis (Fig. 2.4):

$$\nu = -\frac{\epsilon_1}{\epsilon_3} = -\frac{S_1}{S_3} = \frac{C_{12}}{C_{11} + C_{12}} \quad 2.16$$

The values of  $\nu$  ranges from 0.5 down to -1. The maximum value describes an absolute conservation of the volume when applying a uniaxial pressure. A negative value expresses a collapsing of the solid body and can be observed in several complex polymers and in intermediate valent single crystals [5-7]. For polymers it is an effect of their complex geometry, whereas for intermediate valent materials, with their often very simple chemical structure, this behavior is due to their special electronic structure (see also chapter 6).

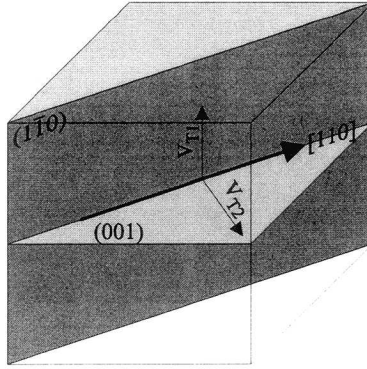


**Fig. 2.5** For a transversal wave, propagating in  $[110]$  direction, there are two different sound velocities depending on the displacement.

### 2.2.3 Anisotropy

For a transverse acoustic wave, propagating in a  $[110]$  direction, there are different sound velocities depending on the direction of the displacement (Fig. 2.5). In a cubic system the two sound velocities  $v_{T_1}$  and  $v_{T_2}$  are given by Eq. 2.24 and Eq. 2.25 . The anisotropy is then defined as [1, 2]:

$$\eta = \left[ \frac{v_{T_1}}{v_{T_2}} \right]^2 = \frac{2 \cdot C_{44}}{C_{11} - C_{12}} \quad 2.17$$

If the value of the anisotropy equals 1 ( $v_{T_1} = v_{T_2}$ ), the crystal is elastically isotropic and directions can not be distinguished elastically. The knowledge of  $\eta > 1$  or  $\eta < 1$  is important for the calculation of the velocity of a surface acoustic wave since the angular dispersion relation depends strongly on it (see also section 2.5).



## 2.3 Wave equation

The dynamics in a solid body is described by the wave equation. To derive it one starts with Newton's law  $F_i = m \cdot \frac{\partial^2 u_i}{\partial t^2}$  [1]. The mass  $m$  can be replaced by the volume integral of the density  $\rho$  and, when external body forces are neglected, the force  $F_i$  can be written as the surface integral of the stress  $\sigma_{ij}$ . Then, Newton's law becomes:

$$\oint_{\partial s} \sigma_{ij} \cdot ds_j = \int_{\delta V} \rho \frac{\partial^2 u_i}{\partial t^2} dV \quad 2.18$$

Using Gauss' theorem this integral equation can be changed easily in its differential form:

$$\nabla_j \cdot \sigma_{ij} = \rho \frac{\partial^2 u_i}{\partial t^2} \quad 2.19$$

The stress can now be expressed by the strain (Eq. 2.3). With the symmetry of the elastic constants and the definition of the strain (Eq. 2.1), Eq. 2.19 takes then the form of the wave equation for a solid body [1-3]:

$$\rho \frac{\partial^2 u_i}{\partial t^2} = c_{ijkl} \frac{\partial^2 u_j}{\partial x_k \partial x_l} \quad 2.20$$

## 2.4 Bulkwaves

The simplest solutions of the wave equation (Eq. 2.20) are bulk waves. The general acoustic wave is a superposition of three independent plane waves. The displacement vectors of such plane waves are perpendicular to each other. For propagation in special crystallographic directions the set of independent plane waves consists of one longitudinal and two transverse or shear waves. Their propagation velocities can be easily calculated. E.g. in a cubic body they are given by [2]:

**Propagation along [100] direction:**

In this case the shear modes are degenerate and the velocities are:

$$v_L = \sqrt{\frac{C_{11}}{\rho}} \quad 2.21$$

$$v_T = \sqrt{\frac{C_{44}}{\rho}} \quad 2.22$$

**Propagation along [110] direction:**

Here the transverse modes are not degenerate because the displacement of the first mode points into the [001] direction whereas the one of the second one points into  $[1\bar{1}0]$ :

$$v_L = \sqrt{\frac{C_{11} + C_{12} + 2C_{44}}{2\rho}} \quad 2.23$$

$$v_{T_1} = \sqrt{\frac{C_{44}}{\rho}} \quad 2.24$$

$$v_{T_2} = \sqrt{\frac{C_{11} - C_{12}}{2\rho}} \quad 2.25$$

**Propagation along [111] direction:**

Once more the transverse waves are degenerate:

$$v_L = \sqrt{\frac{C_{11} + 2C_{12} + 4C_{44}}{3\rho}} \quad 2.26$$

$$v_T = \sqrt{\frac{C_{11} - C_{12} + C_{44}}{3\rho}} \quad 2.27$$

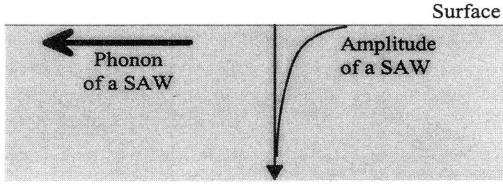


Fig. 2.6 SAW propagating along the surface with an exponentially damped amplitude

## 2.5 SAW in a semi infinite material

Beside the simple bulk waves there are so called surface acoustic waves (SAW) as solution of the wave equation (Eq. 2.20). This sort of waves propagates along surfaces and their displacement fields are localized in the vicinity of the surface.

There are several types of surface waves. The first type discovered was a surface acoustic wave on the stress-free planar surface of a semi infinite, elastically isotropic medium. These waves, called after their discoverer Lord Rayleigh [8], propagate along the surface of the solid, but their amplitudes decay exponentially with increasing distance perpendicular to the surface (Fig. 2.6). Stoneley [9] extended the theory to anisotropic materials. He found a whole class of solutions, which are now known as *generalized Rayleigh waves*.

### 2.5.1 Rayleigh type solution

The general solution of the wave equation (Eq. 2.20) are plane waves given by the real part of:

$$\mathbf{u} = \boldsymbol{\alpha} \cdot \exp[i\mathbf{q} \cdot (\mathbf{l} \cdot \mathbf{x} - vt)] \quad 2.28$$

where  $\boldsymbol{\alpha}$  is the vector of the amplitude,  $q$  is the length of the wave vector  $\mathbf{q}$  and the vector  $\mathbf{l}$  is given by  $l_i = q_i/q$ . To determine the sound velocity  $v$  for a given  $\mathbf{q}$  or vice versa, Eq. 2.28 is entered into Eq. 2.20, which leads to a homogeneous set of

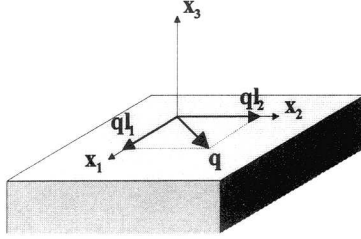


Fig. 2.7 Coordinate system for the surface wave system.

equations (Christoffel equation) [4, 10]:

$$(\Gamma_{ij} - \delta_{ij} \cdot \rho v^2) \cdot \alpha_i = 0 \quad j = 1, 2, 3 \quad 2.29$$

with  $\Gamma_{ij} = l_k l_l \cdot c_{kijl}$  and  $\delta_{ij}$  is the Kronecker function. Then the determinant of Eq. 2.29

$$|\Gamma_{ij} - \delta_{ij} \cdot \rho v^2| = 0 \quad 2.30$$

defines a cubic equation in  $v^2$  and its roots are the squared velocities of three orthogonal waves. In an infinite medium with no further boundary conditions these are the three well known bulk waves, one quasilongitudinal and two quasitransverse.

To get surface waves, the boundary conditions of a semi infinite medium have to be added. For a Rayleigh type surface wave the first boundary condition is a stress-free surface, which can be expressed by [9, 10]:

$$\sigma_{3i} = c_{3ijk} \cdot \frac{\partial u_j}{\partial x_k} \Big|_{x_3=0} = 0 \quad \text{for } i = 1, 2, 3 \quad 2.31$$

and the second one is an exponential damping of the wave perpendicular to the plane surface. To satisfy these boundary conditions (Eq. 2.31) the solution must be a superposition of the waves defined by Eq. 2.28, where all amplitudes vanish with increasing distance from the surface. The coordinate system is chosen so that the axes  $x_1$  and  $x_2$  lie in the surface (Fig. 2.7) and the plane normal is given by  $x_3$ . The wave vector of the propagating surface wave is now defined in the  $(x_1, x_2)$ -plane by

its magnitude  $\mathbf{q}$  and its projection  $ql_1$  and  $ql_2$  (Eq. 2.28). Then one component of the superposition can be written as:

$$\mathbf{u} = \boldsymbol{\alpha} \cdot \exp(-qb x_3) \cdot \exp(iq(l_1 x_1 + l_2 x_2 - vt)) \quad 2.32$$

where  $b \equiv i \cdot l_3$  is a damping constant. In the following the damping term is treated as belonging to the amplitude and only the second exponential term of Eq. 2.32 describes the propagation of the wave. The value of  $b$  is initially unknown, whereas the values of  $l_1$  and  $l_2$  are given by the direction of propagation.

The secular equation Eq. 2.30 can be regarded as a function of  $v^2$  with  $b$  as parameter or vice versa. The second approach is preferred for numerical calculations. Because of the real value of  $l_1$  and  $l_2$ , Eq. 2.30 describes an equation of 3<sup>rd</sup> degree in  $b^2$ . Any value of  $v$  and any of its roots  $b$  define a solution in the form of Eq. 2.32. Such a solution satisfies the wave equation (Eq. 2.20), represents a wave travelling in the plane and has a  $b$ -dependence in the  $x_3$ -direction. From the 6 roots of  $b$  only the three with the negative real part can be used to create a superposition of damped waves:

$$\mathbf{u} = \sum_{i=1}^3 A^{(i)} \boldsymbol{\alpha}^{(i)} \cdot \exp(-qb^{(i)} x_3) \cdot \exp(iq(l_1 x_1 + l_2 x_2 - vt)) \quad 2.33$$

Eq. 2.33 has now to satisfy the boundary conditions (Eq. 2.31). Substituting the solution in Eq. 2.31 creates a new set of homogeneous equations in the unknown weighting factor  $A^{(i)}$ . To get a non trivial solution, the determinant of the coefficients has to vanish. The determinant is given by [10]:

$$\begin{aligned} |D_{nm}| &= \left| c_{m3kl} \cdot \alpha_k^{(n)} \cdot l_l^{(n)} \right| \\ &= \left| \alpha_k^{(n)} \cdot [c_{m3k1} l_1 + c_{m3k2} l_2 - i \cdot c_{m3k3} b^{(n)}] \right| = 0 \text{ for } m, n = 1, 2, 3 \end{aligned} \quad 2.34$$

As mentioned above for any randomly chosen velocity  $v$  the corresponding values of  $l_3^{(n)}$ , respectively  $b^{(n)}$ , can be found. But it is very unlikely that the surface wave calculated with Eq. 2.33 satisfies the boundary condition Eq. 2.34. Only in very few cases (e.g. isotropic material), the whole problem can be solved analytically [9–11]. In most cases one has to use a computer program, that tries successive values

for the velocity  $v$  until the boundary conditions are satisfied. This velocity  $v$  is then the velocity of the surface acoustic wave.

### 2.5.2 Angular Dispersion of an anisotropic cubic medium

In an anisotropic crystal the velocity of a Rayleigh surface acoustic wave depends on the surface orientation and the direction of propagation in the plane. The latter is called *angular dispersion*. Its form is determined by the anisotropy  $\eta$  (Eq. 2.17) of the material. In the following the angular dispersion of two prototype materials, single crystal copper ( $\eta > 1$ ) and PbS ( $\eta < 1$ ), will be shown and discussed. The curves are simulations, calculated with the elastic constants and the density of both materials. In general the velocity of a real Rayleigh SAW is smaller than the velocity of any bulk wave [10].

#### (001) plane:

As a consequence of the fourfold symmetry of a (001) surface it is enough to measure the sound velocities in an azimuthal range of  $45^\circ$  from [100] to [110]. In Fig. 2.8 and in Fig. 2.9 the dispersion relation of materials with  $\eta > 1$  and  $\eta < 1$  is plotted. Obviously the behavior of the materials is quite different. Copper with an anisotropy greater than one shows a strong dependence on the direction of propagation. On the other hand the SAW velocity of PbS varies only within a very small range of about 1% and lies about 5% below the  $T_1$  bulk mode [10]. A further significant difference of these two materials is the angle  $\delta$  between the displacement ellipse, defined by the two vectors  $\alpha_\perp$  and  $\alpha_\parallel$  of the SAW displacement, and the sagittal plane, the plane defined by the direction of propagation and the  $x_3$  axis (Fig. 2.10). In the material with  $\eta < 1$ ,  $\delta$  varies only between  $0^\circ$  and about  $7^\circ$ . So the displacement perpendicular to the direction of propagation lies mostly in the sagittal plane. On the other hand, in copper the displacement ellipse of the SAW rotates from  $0^\circ$  for propagation in [100] to  $90^\circ$  for propagation in [110] (Fig. 2.11). In other

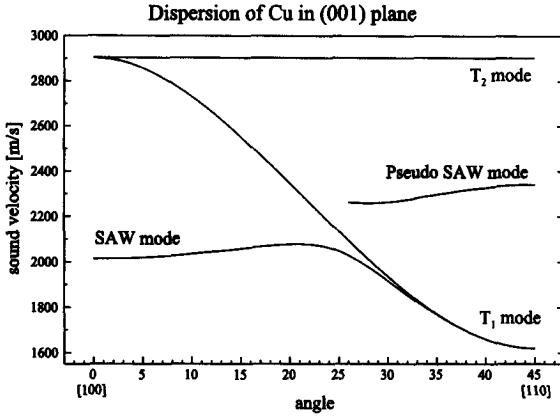


Fig. 2.8 Shear- and surface wave velocities for propagation in a (001) plane of copper. The displacement of the  $T_2$  mode is always perpendicular to the plane, whereas the one of the  $T_1$  lies in the plane. By turning the propagation direction into [110] the velocity of the pure SAW converges to the velocity of the  $T_1$  mode. In the range from about  $26^\circ$  to  $45^\circ$  a so called pseudo SAW can be observed.

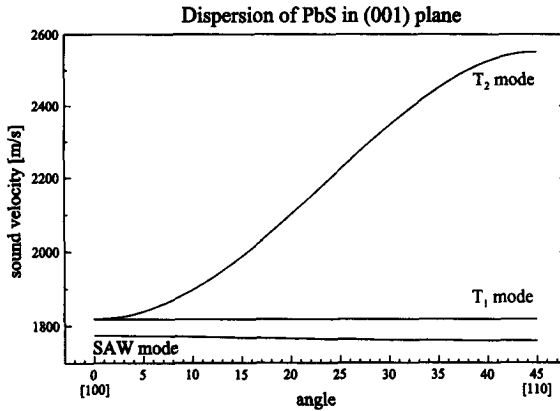


Fig. 2.9 Shear- and surface wave velocities for propagation in a (001) plane of PbS. The displacement of the  $T_1$  mode is always perpendicular to the plane, whereas the one of the  $T_2$  lies in the plane.

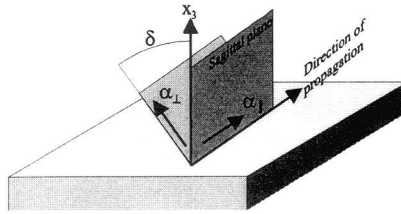


Fig. 2.10 Angle  $\delta$  between the sagittal plane and the displacement plane defined by the displacement  $\alpha_{\perp}$  perpendicular and  $\alpha_{\parallel}$  parallel to the direction of propagation.

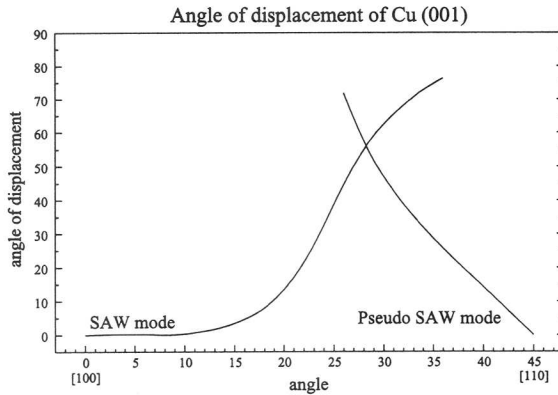
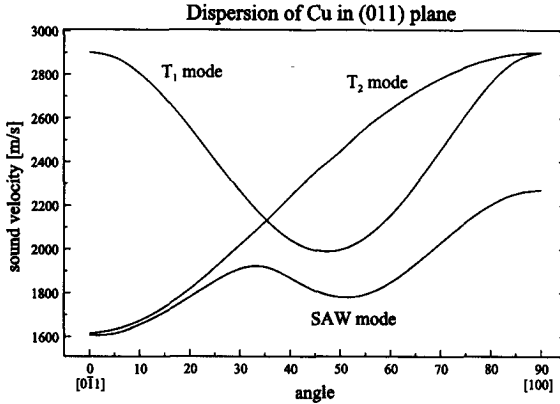


Fig. 2.11 Angle  $\delta$  between the sagittal plane and the displacement ellipse in copper.

words for a SAW travelling along [100] the displacement  $\alpha_{\perp}$  stands perpendicular to the plane whereas along [110] it lies in the plane. As will be explained in chapter 3, light scattering on surface acoustic waves takes only place on so called surface ripples, which are displacements of the surface in the  $x_3$  direction. So when the displacement of the wave lies in the plane it can not be detected by the optical way of Brillouin spectroscopy. And in fact from an azimuthal angle of more than  $25^\circ$  it is nearly impossible to see a pure SAW [10, 12–15].

In Fig. 2.8 also the velocities of a pseudo SAW are plotted. This mode is called





**Fig. 2.12** Shear- and surface wave velocities for propagation in a (011) plane of copper. The SAW velocity is always smaller than the one of the transverse bulk modes.

*pseudo* because only two of its three partial waves are damped and propagate along the plane surface. The third one is not damped and produces therefore an energy flow into the bulk [10]. In Fig. 2.11 the angle  $\delta$  between the displacement ellipse of the pseudo SAW and the sagittal plane is plotted, too. Here the displacement vector  $\alpha_{\perp}$  turns with increasing azimuthal angle from the surface plane into the sagittal plane and thereby it increases the scattering cross section. Indeed from about  $28^{\circ}$  this pseudo SAW can be measured with Brillouin spectroscopy as the scattering on it dominates.

**(011) plane:**

On a cubic (110) plane, because of its two fold symmetry, it has to be measured along a range of  $90^{\circ}$ , from  $[0\bar{1}1]$  to  $[100]$ , to get the whole angular dispersion. In Fig. 2.12 and Fig. 2.13 the SAW velocities of copper and PbS are plotted together with the velocities of the two shear modes. In the (011) plane  $v_{SAW}$  of both materials is strongly depending on the azimuthal angle. But again the two angular dispersion relations look very different depending on the anisotropy. The

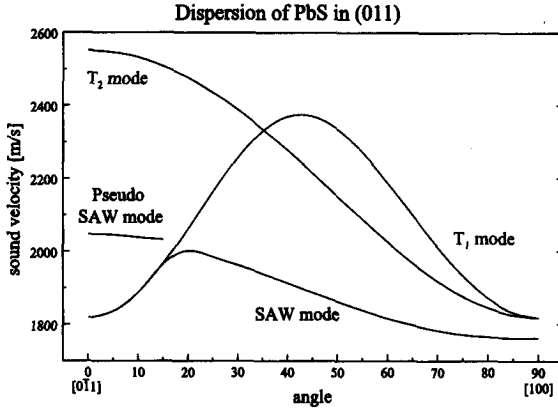


**Fig. 2.13** Shear- and surface wave velocities for propagation in a (001) plane of PbS. The velocity of the pure SAW converts with increasing angle to the  $T_1$  mode. In the range from  $0^\circ$  to about  $20^\circ$  only a pseudo SAW is observed, but not the pure mode

angle of the displacement ellipse of copper varies now between about  $35^\circ$  and  $-18^\circ$  and a pure SAW can be measured over the whole angular range. In PbS with  $\eta < 1$  the displacement ellipse of the pure SAW lies for propagation in the  $[0\bar{1}1]$  direction in the surface plane and only a pseudo SAW can be detected [10]. At an angle of about  $20^\circ$  from the  $[0\bar{1}1]$  direction the pure SAW displacement component in the sagittal plane becomes big enough to enable the observation of the pure Rayleigh surface acoustic wave.

### (111) plane:

On a (111) plane the surface acoustic waves do not depend on the anisotropy. For both materials, copper and PbS, the angular dispersion shows the same form (Fig. 2.14). One has to look only at propagation directions from  $[\bar{1}10]$  to  $[\bar{1}22]$  (range of  $30^\circ$ ) due to the symmetry.

The angle  $\delta$  of the displacement ellipse to the sagittal plane is for all materials smaller than  $45^\circ$  along  $[\bar{1}10]$  and becomes  $\delta = 0$  along  $[\bar{1}22]$ .

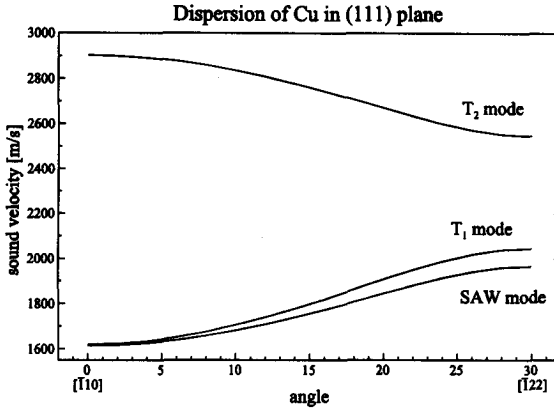
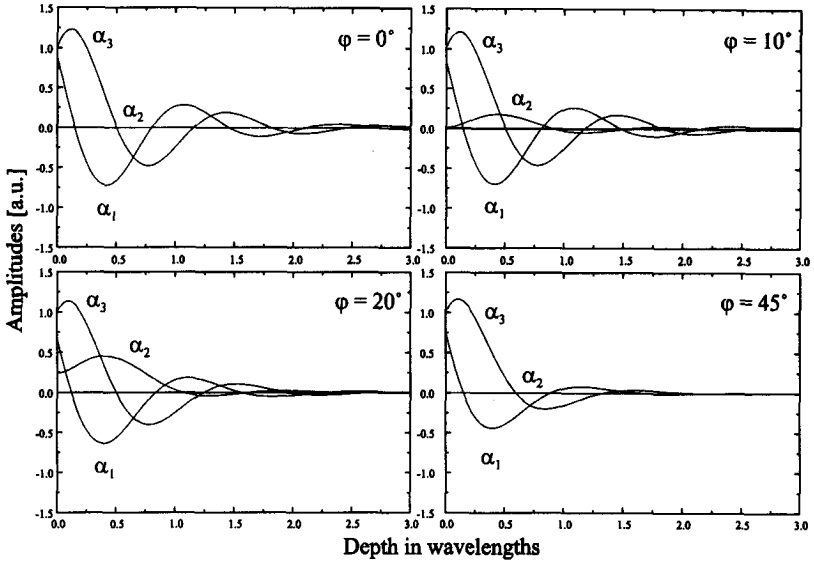


Fig. 2.14 Shear- and surface wave velocities in a (111) copper plane. In the (111) plane the angular dispersion is identical for materials with anisotropy  $\eta < 1$  or  $\eta > 1$ .

### 2.5.3 Amplitude of a SAW

Beside travelling along the surface, the amplitude of a surface acoustic wave intrudes into the bulk material. The depth of this penetration depends on the damping constants  $b^{(n)}$  (Eq. 2.32). In Fig. 2.15 all three components of the displacement amplitudes are plotted for different azimuthal angles in the (001) copper plane. It can be clearly seen, that still up to two wavelengths ( $\lambda_{Laser} = 514.5$  nm) the displacement can not be neglected. For other materials or different oriented surfaces the damping can even be much less and the penetration depth is much larger. Therefore surface acoustic waves are probing, despite of their surface nature, the bulk material, as well [16].



**Fig. 2.15** The components of the displacements are plotted versus increasing distance (in wavelengths of the detecting Laser,  $\lambda = 514.4$  nm) into the solid of copper from the  $[001]$  surface at a fixed time.  $\varphi$  is the azimuthal angle measured from  $(100)$ . The plots with  $\varphi = 0^\circ, 10^\circ$  and  $20^\circ$  show a pure Rayleigh SAW, whereas the one with  $\varphi = 45^\circ$  shows a pseudo SAW. Up to two wavelengths ( $\approx 1\mu\text{m}$ ) there are significant amplitudes.

## 2.6 SAW in a thin film

Beside single crystals with a cleaved surface thin films with thickness of about  $100 - 10000 \text{ \AA}$  on a substrate are also very interesting. As shown in the previous section, the penetration depth of a SAW is more than  $1 \mu\text{m}$ , therefore when examining a thin film the substrate must not be neglected [12, 17]. On the other hand, a material coated with a thin film, can still be measured with surface acoustic waves, when the coating is not too thick ( $< 1000 \text{ \AA}$ ) [6, 7, 18, 19]. Of course both materials have an influence on the surface acoustic wave and have to be taken into consideration.

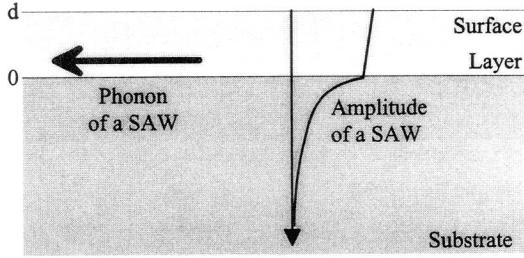


**Fig. 2.16** A surface acoustic wave propagates along the plane surface with a displacement in both, the thin film and the underlying substrate.

To deal with the complication of the thin film, the wave (Eq. 2.33) has to be divided into two parts [17]:

$$\mathbf{u} = \begin{cases} \mathbf{u}^{Layer} & \text{for } 0 < x_3 \leq d \\ \mathbf{u}^{Substrate} & \text{for } x_3 \leq 0 \end{cases} \quad 2.35$$

Where  $d$  is the thickness of the layer on the substrate (Fig. 2.16). Both,  $\mathbf{u}^{Layer}$  and  $\mathbf{u}^{Substrate}$  have to fulfill independently the wave equation (Eq. 2.20) with the elastic stiffness constants and the density of either the thin film or of the substrate, respectively. While in the bulk the displacement  $\mathbf{u}$  must describe a damped wave, in the thin film this is not necessarily so [17]. Therefore, the general solution in the layer consists of a superposition of six waves depending on all six roots  $l_3^{(n)}$  of Eq. 2.30. As was described in section 2.5.1 of this chapter, in the bulk body only the three roots  $b$  ( $\equiv i \cdot l_3$ ) with negative real part can be used to build the necessary damped wave.

Two additional conditions for  $x_3 = d$  are added to the boundary condition of the stress-free surface ( $x_3 = 0$ ) (Eq. 2.31): continuity of the stress and of the displacement at the interface between the thin film and the bulk [17].

$$u_i^{Layer} = u_i^{Substrate} \Big|_{x_3=0} \quad 2.36$$

$$\sigma_{3i}^{Layer} = \sigma_{3i}^{Substrate} \Big|_{x_3=0} \quad 2.37$$

Putting the Ansatz (Eq. 2.33) in the boundary conditions (Eq. 2.31, Eq. 2.36 and Eq. 2.37) a new set of 9 homogeneous linear equations are created. As described in section 5.1 of this chapter, the sound velocity  $v_{SAW}$  will then be found numerically in a way, that the determinant of the boundary condition matrix vanishes.

### 2.6.1 Angular dispersion

In isotropic systems, one distinguishes two different sorts of surface acoustic waves. The first, called *Love waves* [17], describe a surface wave with displacement only perpendicular to the sagittal plane. The second are called *generalized Lamb- or Rayleigh type waves* [17]. Their displacement ellipse lies always in the sagittal plane.

In an anisotropic material this clear distinction can not be done any more. Here the displacement ellipse changes its angle to the sagittal plane depending on the direction of propagation. The SAW in an anisotropic semi infinite medium behaves in the same way. Therefore every Love wave gets a component, that lies in the sagittal plane and, vice versa, every Rayleigh like surface acoustic wave has a component of the displacement vector perpendicular to the sagittal plane, too.

### 2.6.2 $qd$ -dispersion

In contrast to the solution of a semi infinite body, in a thin layer on a substrate the velocity of a surface acoustic wave depends strongly on the thickness  $d$  of the thin film and of the  $q$ -vector. Because  $d$  and  $q$  appear only as product  $qd$  in the solution, the velocity can be plotted against  $qd$  (Fig. 2.17). The behavior of the velocity in the  $qd$ -dispersion depends on the velocity of the shear waves of both, the substrate material and the material of the thin film. Three cases can be distinguished:

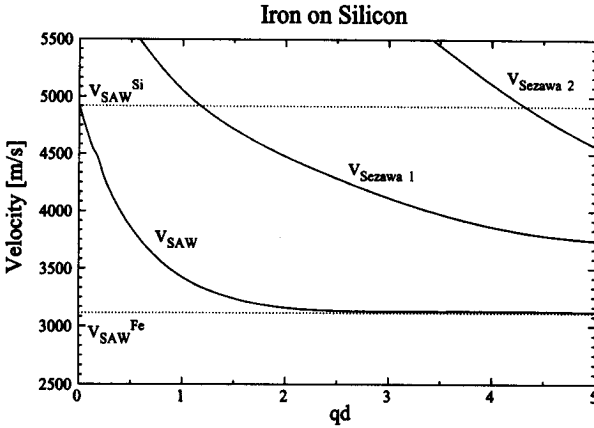


**Fig. 2.17** Velocities of Rayleigh type surface acoustic waves on a silicon substrate with a thin Fe film propagating along  $[100]$  in a  $(001)$  plane. Beside the Rayleigh SAW, two Sezawa modes are plotted.

$$v_T^{Layer} > v_T^{Substrate};$$

In this case the substrate is *stiffened* by the film. Starting from the value of  $v_{SAW}^{Substrate}$  at  $qd = 0$  the velocity of the surface acoustic wave increases monotonically with  $qd$ . There exists only *one* Rayleigh like mode [17, 19]. The increase of  $v_{SAW}$  is limited by the shear velocity in the substrate, which lies always over  $v_{SAW}^{Substrate}$ . For values larger than the cutoff value  $qd_{Cutoff}$  no propagating surface acoustic wave can be found.

$$v_T^{Layer} < v_T^{Substrate};$$

Here the layer *loads* the substrate and the velocity of the surface acoustic wave decreases with increasing  $qd$ . As before the limit for  $qd \rightarrow 0$  is  $v_{SAW}^{Substrate}$ , but for  $qd \rightarrow \infty$  the surface acoustic wave converts asymptotically to  $v_{SAW}$  of the thin film. Beside this solution there exists a whole set of other Rayleigh type waves, called *Sezawa modes* (Fig. 2.17) [17]. In contrast to the Rayleigh solution all Sezawa

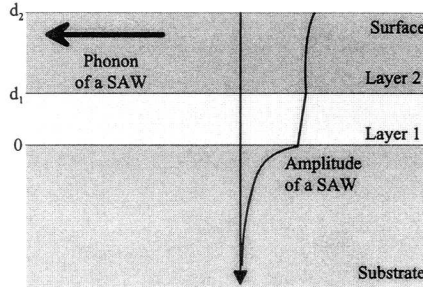


Fig. 2.18 A surface acoustic propagating along the plane surface in a multi layer system.

modes have a cutoff value of  $qd$ , below that the mode does not appear.  $qd_{Cutoff}$  of each mode is higher than the previous one. For  $qd \rightarrow qd_{Cutoff}$  the Sezawa velocity approaches to the shear velocity of the substrate. At large values of  $qd$  the velocity of a Sezawa mode tends to the shear velocity of the layer.

$$v_T^{Layer} \approx v_T^{Substrate};$$

When the shear velocities of both, the substrate and the layer, are similar, so called *Stoneley* waves can occur [17]. This mode is dispersionless and does not exactly describe a surface acoustic wave, but a wave propagating along the interface between both materials. Its amplitudes decay exponentially within a few wavelengths on both sides of the interface.

## 2.7 SAW in a multi-film-system

The theory of an elastic wave propagating in a thin film on a substrate can easily be extended to a system with several thin layers. In each layer and in the substrate the wave equations (Eq. 2.20) are solved for its own and the different solutions are



connected together by the boundary conditions, the continuity of the displacement and of the stress at the interfaces (Eq. 2.36, Eq. 2.37). As in section 2.5 the surface must be stress-free (Eq. 2.31) and the amplitude in the substrate must vanish with increasing distance from the surface.

The number of possible wave modes increases with the complexity of the system. For example, besides all the wave modes described in section 2.6, a wave can be guided in a layer between two interfaces with a damped displacement amplitude on the other side of the interface.

### 2.7.1 Superlattice on a substrate

A special case of a multi-film-system are superlattices. On a substrate two or more different layers are periodically repeated with always the same film thickness. It is obvious, that already a few periods (10 or more) increases the complexity of the boundary conditions matrix enormously. Remember that, each interface, between two layers or between a layer and the substrate, adds *six* additional boundary conditions and the expense to calculate the determinant is at least proportional to the square of the number of boundary conditions [20]!

But, because a single layer in such a system is normally only a few Ångstroms thick, it is allowed to replace the periodic layer-system by one homogeneous layer with one set of elastic constants and one density. Whereas the density is the average of all densities weighted by the layer thickness, the elastic constants can not be calculated easily from the elastic constants of the layer materials.

When the density and the elastic constants of the average film are known, the velocity of the surface acoustic waves can be calculated as described in section 2.6 and therefore the average elastic constants can be calculated from the measured angular or  $qd$  dispersion of the film.

# Chapter 3

## Brillouin spectroscopy

Independently from each other, Brillouin in 1922 [21] and Mandelstam in 1926 [22] predicted the inelastic scattering of light on thermally excited acoustic phonons. Because of the very small energy shift ( $\Delta f \leq 100$  GHz), only the invention of the laser and the use of high resolution Fabry-Pérot interferometers [23] made it possible to observe this scattering. In the mean time the technique of Brillouin spectroscopy has become a powerful tool for the examination of acoustic phonons [4, 12, 24] as well as for other excitations in a solid body with a very small energy shift (e.g. spin-waves [25]).

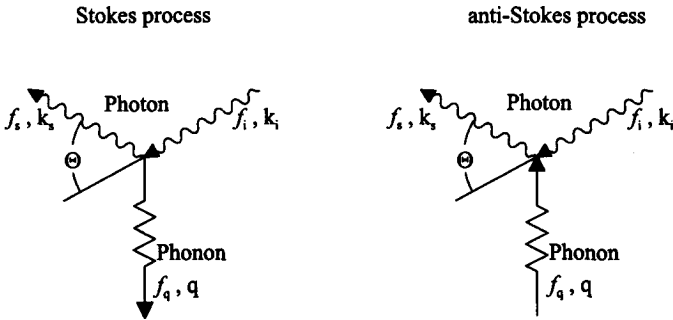


**Fig. 3.1** The picture on the left shows a Stokes process, where a phonon with the frequency  $f_q$  and the wavevector  $q$  is created by an incident photon with frequency  $f_i$  and wavevector  $k_i$ . The photon, scattered under an angle  $\Theta$ , has a frequency  $f_s$  and a wavevector  $k_s$ . The picture on the right shows the inverse process (anti-Stokes), where a phonon is annihilated.

### 3.1 Inelastic light scattering on acoustic phonons

In a quantum mechanical picture the first order scattering of light on phonons can be expressed by the creation or annihilation of a phonon by photons. The creation is called Stokes process and the scattered photon has a slightly smaller energy than the incident one. The annihilation is called the anti-Stokes process with a shift to higher photon energy (??). The energy and the momentum of the created or annihilated phonon can be easily calculated from the conservation of energy and momentum [12, 26]:

$$\hbar f_i = \hbar f_s \pm \hbar f_q \quad 3.1$$

$$\hbar \mathbf{k}_i = \hbar \mathbf{k}_s \pm \hbar \mathbf{q} \quad 3.2$$

where the index  $i$  and  $s$  stands for the incident respectively the scattered photon and  $q$  for the phonon. The  $f$  are the frequencies, while  $\mathbf{k}$  and  $\mathbf{q}$  are the wave vectors. The upper sign stands for a creation of a phonon, the lower for annihilation.

Due to the very small difference in the energies of the incident and the scattered photon, the  $k$ -vector remains constant:  $|\mathbf{k}_i| \simeq |\mathbf{k}_s| = k$ . Then the length of the phonon wave vector  $\mathbf{q}$  can be expressed by [27]

$$q = 2 \cdot k \cdot \sin\left(\frac{\Theta}{2}\right) \quad 3.3$$

Obviously  $q$  becomes maximal when  $\Theta = 180^\circ$ , which is equivalent to an exact backscattering geometry. Nevertheless, the maximum value of  $q$ , for scattering photons in the visible range, is still very small compared with a  $k$ -vector lying at the border of the first Brillouin zone. The ratio is about

$$\frac{q}{k_{1.BZ}} \approx \frac{1}{500} \quad 3.4$$

Therefore the scattering takes place very near the middle of the Brillouin zone ( $\Gamma$  point). But in this case the group velocity of a phonon is equal to its phase velocity,

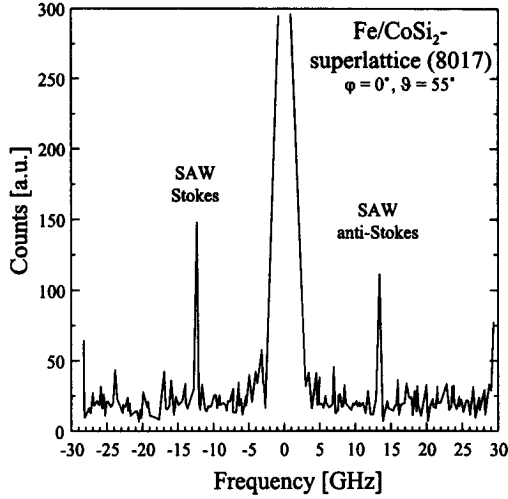


**Fig. 3.2** A typical Brillouin spectrum. The sample was an epitaxially grown, (111) oriented, 340 Å thick Fe/CoSi<sub>2</sub> superlattice on a (111) Si substrate. Clearly visible are the needle like peaks created by the Stokes and anti-Stokes process.

which can be assumed as constant.

$$\frac{d\omega}{dk} = \frac{\omega}{k} = \text{const.} \quad 3.5$$

Then, the velocity of the phonon can be calculated from the measurable frequency shift of the scattered photon by

$$v_q = \frac{\lambda \cdot \Delta f}{2 \cdot \sin(\Theta/2)} \quad 3.6$$

where  $\lambda$  is the wavelength of the photon and  $\Delta f = f_i - f_s$  is its frequency shift. For scattering on surface acoustic phonons only components of the wave vectors parallel to the surface are of interest. Then, in exact backscattering geometry Eq. 3.6 becomes

$$v_q = \frac{\lambda \cdot \Delta f}{2 \cdot \sin(\vartheta)} \quad 3.7$$

where  $\vartheta$  is the angle of the incident photon measured from the surface plane normal.

In Fig. 3.2 a typical Brillouin spectrum is plotted. It is dominated by the peak of the elastic scattered light at  $\Delta f = 0$  GHz. The inelastic scattering on phonons creates two further peaks. One at lower frequencies (Stokes process) and one at higher frequencies (anti-Stokes process).

## 3.2 Cross section on surface acoustic waves

### 3.2.1 Mechanism of scattering

There are two different, fundamental scattering mechanisms. Which mechanism dominates, depends on where the scattering takes place, inside the medium or at its surface. In the first case the bulk phonons create inside the solid body fluctuations of the dielectric function [28]

$$\epsilon_{ij}^{in}(\mathbf{r}, t) = \epsilon_{ij}^0 + \delta\epsilon_{ij}(\mathbf{r}, t) \quad 3.8$$

Generally this equation is only true in the Fourier space, since  $\epsilon_{ij}^0$  is a function of  $\mathbf{k}$  and  $\omega$ , but here monochromatic light with a fixed frequency  $\omega$  is assumed and therefore Eq. 3.8 becomes perfectly true. Eq. 3.8 describes the elasto-optic contribution to the scattering. The fluctuation term can be described as

$$\delta\epsilon_{ij} = k_{ijkl} \cdot \epsilon_{kl} \quad 3.9$$

where  $k_{ijkl}$  are the elasto-optic coefficients and  $\epsilon_{kl}$  is the strain as defined in Eq. 2.1.

A competitive mechanism is the scattering on a mechanical perturbation of the surface, on so called surface-ripples (Fig. 3.3). The ripples are produced by surface acoustic waves with a displacement vector perpendicular to the surface (compare

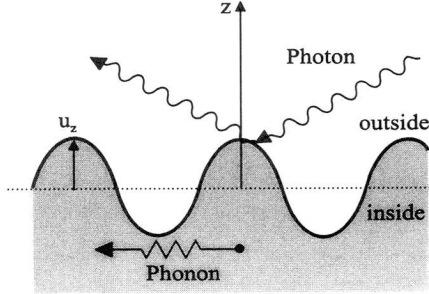


**Fig. 3.3** Scattering on surface ripples.  $u_z$  defines the displacement of the surface from an equilibrium position.

with chapter 2). The total dielectric function can then be written as [28]

$$\epsilon_{ij}(\mathbf{r}, t) = \delta_{ij} \cdot \theta[\mathbf{r}_\perp - u_z(\mathbf{r}_\parallel, t)] + \epsilon_{ij}^{\text{in}}(\mathbf{r}, t) \cdot \theta[u_z(\mathbf{r}_\parallel, t) - \mathbf{r}_\perp] \quad 3.10$$

where  $\delta_{ij}$  is the Kronecker function,  $\theta$  a Heaviside step function and  $u_z$  the displacement of the surface. The first term describes the dielectric function outside the medium, the second inside.

Which mechanism dominates the scattering process, depends on the optical properties of the medium. The elasto-optic cross section ( $d\sigma^2/d\Omega d\omega$ ) is proportional to the transmission function at the surface and inversely proportional to the squared optical absorption, when the absorption is large. On the other hand, the cross section of the ripple mechanism is proportional to the reflectivity [29]. Therefore on opaque samples with high absorption and high reflectivity coefficient, the scattering on the surface-ripples dominates.

### 3.2.2 Polarization and incident angle of the light

Whereas the polarization of the incident light has no significant influence in the

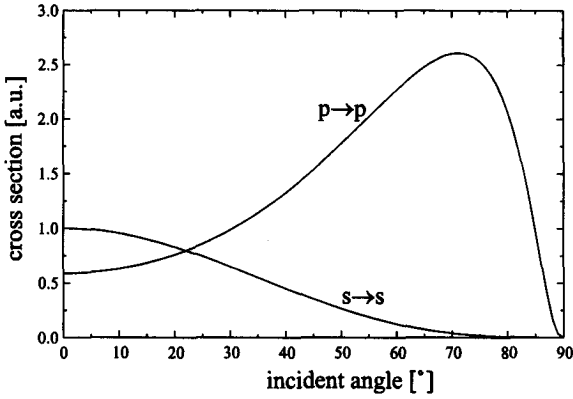


**Fig. 3.4** Cross section depending on the polarisation of the light and the incident angle (measured from the plane normal). The cross section of  $p \rightarrow p$  scattering has a clear maximum at about  $70^\circ$ . The exact value depends on the reflectivity. The cross section of  $s \rightarrow s$  scattering vanishes in this region of large  $k$ -vectors (= large incident angle).

cross section of the elasto-optic scattering, the scattering on surface-ripples depends strongly on the polarization (p, s) and the incident angle of the light ( $\Theta$ ) (Fig. 3.4). The cross section is then in the back scattering geometry proportional to [28,30,31]:

$$\left( \frac{d\sigma^2}{d\Omega \cdot d\omega} \right)_{p \rightarrow p} \sim \frac{\cos^3 \vartheta}{(\cos \vartheta + (\epsilon^0)^{-1/2})^4} \cdot \left| 1 + (\epsilon^0)^{-3/2} \cdot \sin \vartheta + \sin^2 \vartheta \right|^2 \quad 3.11$$

$$\left( \frac{d\sigma^2}{d\Omega \cdot d\omega} \right)_{s \rightarrow s} \sim \cos^3 \vartheta \cdot \left| 1 + (\epsilon^0)^{-3/2} \cdot \sin \vartheta \right|^2 \quad 3.12$$

$$\left( \frac{d\sigma^2}{d\Omega \cdot d\omega} \right)_{\substack{s \rightarrow p \\ p \rightarrow s}} \sim \cos \vartheta \cdot \left| (\epsilon^0)^{-3/2} \cdot \sin \vartheta \right|^2 \quad 3.13$$

Where  $\epsilon^0$  is the dielectric function.

Only the cross section of  $p \rightarrow p$  scattering - p means that the light is polarized parallel to the sagittal plane - has a maximum in the interesting range of large  $k$ -vectors. The maximum lies around  $70^\circ$  depending on the reflectivity  $R(\epsilon^0)$ . The cross section of  $s \rightarrow s$  scattering is already much less and vanishes in the interesting  $k$ -vector region. For scattering, that changes the polarization ( $p \rightarrow s$  and  $s \rightarrow p$ ) the

---

cross section becomes negligibly small.

### **3.2.3 Thermal influence**

For the cross section on surface ripples the influence of the temperature is linear for all polarizations [28,31].

### **3.2.4 Conclusions**

The best way to perform Brillouin spectroscopy on surface acoustic waves, is the use of high reflecting samples like a metal in an exact back scattering geometry. The monochromatic light should be polarized parallel to the sagittal plane (p-polarization) and the optimal angle under which the sample is hit by the laser beam, is around  $70^\circ$ .



Leer - Vide - Empty

# Chapter 4

## Experimental details

As mentioned in the previous chapter, the energy of acoustic phonons and therefore also the frequency shift of the scattered light, detectable by visible light, lies in a range from 0 GHz up to about 100 GHz (measured in the frequency equivalence). These energies are very small compared with the frequency of visible light ( $f \approx 500$  THz). The resolutions of the best grating spectrometers, used for Raman spectroscopy, are in wave numbers about 1/cm. This corresponds to about 30 GHz. It is obvious, that this is far away from the resolution needed for Brillouin spectroscopy. For that purpose Fabry-Pérot interferometers are used.

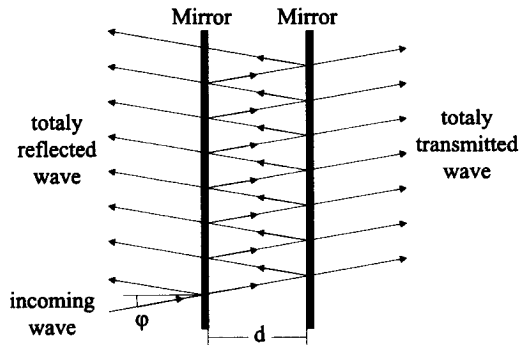


Fig. 4.1 A Fabry-Pérot acts as a very narrow band filter. For wavelengths, which fulfill  $d \cdot \cos(\varphi) = \frac{\lambda}{2} m$ , the transmission through both high reflecting mirrors is 100%!

## 4.1 3+3-pass Fabry-Pérot interferometer

### 4.1.1 Principle of a Fabry-Pérot

In general a Fabry-Pérot (FP) consists of two high reflecting, parallel mounted mirrors (Fig. 4.1) [23, 32, 33]. One part of the incident wave is reflected and the other, much smaller part is transmitted through the first mirror (mirror losses are neglected). On the second mirror the same happens again. But now the reflected light beam is trapped between the two mirrors. Each time the wave is reflected on a mirror a small part of the light is transmitted and interferes with either the totally reflected or transmitted wave (Fig. 4.1). If the condition

$$d \cdot \cos(\varphi) = \frac{\lambda_m}{2} \cdot m \quad 4.1$$

is satisfied, the interference of the transmitted wave is constructive and for the reflected one destructive.  $d$  is the mirror spacing,  $\lambda_m$  the wavelength of the light,  $\varphi$  the angle of the incident beam and  $m$  a positive integer value. In Fig. 4.2 the transmission is plotted versus the phase shift  $\Delta\Phi = 2kd \cdot \cos(\varphi) = 2\frac{2\pi}{\lambda}d \cdot \cos(\varphi)$ . Obviously the phase shift depends on the wavelength  $\lambda = c/f$  ( $f$  = frequency) and the mirror spacing  $d$ . Therefore the FP acts as a narrow band frequency filter tunable by the mirror spacing  $d$ . In the following discussion the beam hits the mirror always perpendicular ( $\varphi = 0$ ). Then the resulting transmission becomes [32]:

$$T_{res} = T_{max} \cdot \frac{1}{1 + \left(\frac{2F}{\pi}\right)^2 \cdot \sin^2\left(\frac{\Delta\Phi}{2}\right)} \quad 4.2$$

where  $F = \pi\sqrt{R}/(1 - R)$  is called the *finesse* and  $R$  is the reflectivity. This definition of the *ideal* finesse is only true for perfectly plane and parallel mounted mirrors. Because of defects and imperfections, the effective finesse becomes smaller

Number of FP	Number of passes	R	F	$\frac{\delta\nu}{\Delta\nu}$	$C_{\frac{max}{min}}$	$C_{\frac{2\pi m}{2\pi(m\pm 1)}}$
1	1	0.94	50.7	0.020	$10^3$	1
1	1	0.85	19.3	0.052	$10^2$	1
1	1	0.99	312.6	0.003	$4 \cdot 10^4$	1
2	1+1	0.94	50.7	0.013	$10^6$	$10^2$
2	3+3	0.94	50.7	0.007	$10^{18}$	$10^6$

**Table 4.1** Properties of different interferometer configurations (one or two Fabry-Pérots, different reflectivity of the mirrors and different number of passes through each FP). The last row shows the parameters of the used Fabry-Pérot interferometer.  $R$  is the reflectivity,  $F$  the finesse,  $\frac{\delta\nu}{\Delta\nu}$  the resolution,  $C_{\frac{max}{min}}$  the contrast and  $C_{\frac{2\pi m}{2\pi(m\pm 1)}}$  the contrast between two neighbouring maxima

and can be expressed by [33]

$$\frac{1}{F_{eff}} = \frac{1}{F_{ideal}} + \sum_i \frac{1}{F_i} \quad 4.3$$

where  $F_i$  are the contribution of the imperfections.

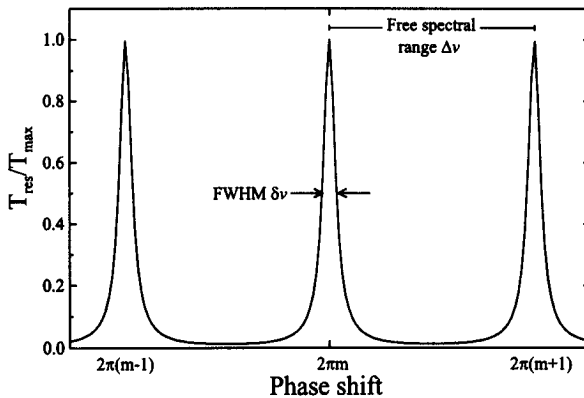


**Fig. 4.2** The transmission function as a function of the phase shift. For the calculation a reflectivity of only  $R = 0.8$  was chosen to improve the visibility of the details. The free spectral range defines the space between to peaks and is equivalent to a phase shift  $\Delta\Phi = 2\pi$ . FWHM is given by  $\delta\nu = 2\pi/F$

For absorption free mirrors the maximal transmission ( $\Delta\Phi = 2\pi \cdot n$ ) becomes  $T_{max} = 1$ .  $T_{res}$  is an Airy function with a *FWHM* (full width at half maximum)  $\delta\nu \simeq 2\pi/F$ . Therefore the finesse is a factor for the quality of the Fabry-Pérot resonator. The larger the finesse and therefore the reflectivity  $R$  becomes, the narrower the transmission peak is! The space between two maxima is called the *free spectral range*  $\Delta\nu$  ( $= 2\pi$  in the phase shift picture). The value of the FWHM can then also be expressed as  $\delta\nu = \frac{1}{F}\Delta\nu$ . The free spectral range and the FWHM can be written as an energy- or a frequency shift instead as a phase shift:

$$\Delta\nu = \frac{c}{2d} \quad 4.4$$

$$\delta\nu = \frac{c}{2dF} \quad 4.5$$

where  $c$  is the speed of light in the medium.

An other important characteristic of a Fabry-Pérot is the contrast between  $T_{max}$  and  $T_{min} = T_{res}(\Delta\Phi = \Delta\nu/2)$ . The contrast is defined as [23]:

$$C_{\frac{max}{min}} = \frac{T_{max}}{T_{min}} = 1 + \left(\frac{2F}{\pi}\right)^2 \sin^2\left(\frac{\Delta\nu}{4}\right) \underset{\Delta\nu=2\pi}{=} 1 + \left(\frac{2F}{\pi}\right)^2 \simeq \left(\frac{2F}{\pi}\right)^2 \quad 4.6$$

In Table 4.1 are the finesse, the resolution and the contrast tabulated for mirrors with different reflectivity  $R$ . It is obvious that the contrast for a single Fabry-Pérot is not large enough to perform successfully Brillouin spectroscopy. The periodical maxima of the transition function are an other problem. It makes it impossible to distinguish between peaks from scattering on low- or high-energy phonons [23]. One way to solve this problem is to enlarge the free spectral range, but then the resolution worsens at the same time .

### 4.1.2 Multipass Fabry-Pérot interferometer

An other and much more elegant way to improve the contrast and to break the periodicity of the resonator, is to use two Fabry-Pérots with different mirror

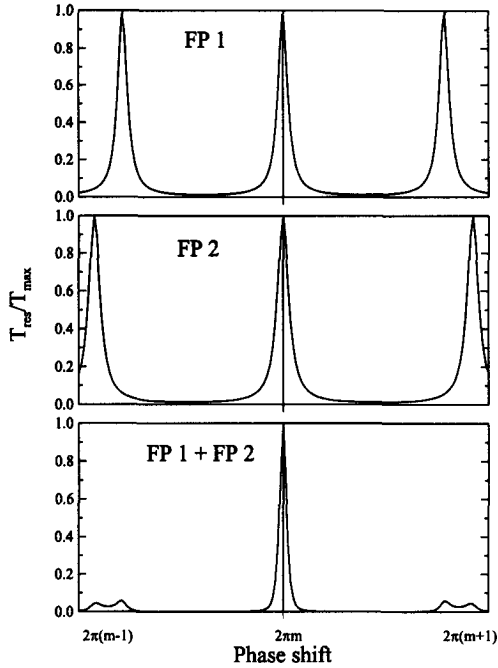


**Fig. 4.3** The top and the middle pictures show the transition function of two Fabry-Pérots with different mirror spacing. In the bottom picture the transition function of the two FPs in a tandem configuration are plotted. Clearly visible are the camel bumps in the range of the first neighbouring transition maxima.

spacings in a tandem constellation. There, the light passes through both FP, which are mounted in a line. The two mirror spacings can be set in a way, that at the desired energy or frequency the transition maxima lie exactly at the same position to each other [27]. Then the total transmission is maximal, too. But, as plotted in Fig. 4.3, the first neighboring peaks of the two transition functions are shifted a little bit to each other and there the total transmission function looks like a *camel bump*. Analytically the tandem transition function is the multiplication of the two

single FP transition functions:

$$T_{\text{tandem}}(\Delta\Phi) = T_{\text{res},1}(\Delta\Phi) \cdot T_{\text{res},2}(\Delta\Phi) = T_{\text{res}}(\Delta\Phi) \cdot T_{\text{res}}(\Delta\Phi \cdot \gamma) \quad 4.7$$

where  $\gamma = d_1/d_2$ . The contrast of the camel bumps to the transition maximum can then be defined as:

$$C_{\frac{2\pi m}{2\pi(m\pm 1)}} = \frac{T_{\text{tandem}}(2\pi m)}{T_{\text{tandem}}(2\pi(m\pm 1))} \quad 4.8$$

To further improve the resolution and the contrast of such a tandem setup, the light can pass the Fabry-Pérot several times. For  $N$  passes through each FP, the transition function, the resolution and the contrast become:

$$T_{\text{total}} = T_{\text{tandem}}^N \quad 4.9$$

$$\frac{\delta\nu}{\Delta\nu_{\text{total}}} = \sqrt{\sqrt[2N]{2} - 1} \cdot \frac{\delta\nu}{\Delta\nu} \quad 4.10$$

$$C_{\frac{\text{max}}{\text{min}},\text{total}} = \left(C_{\frac{\text{max}}{\text{min}}}\right)^{2N} \quad 4.11$$

$$C_{\frac{2\pi m}{2\pi(m\pm 1)},\text{total}} = \left(C_{\frac{2\pi m}{2\pi(m\pm 1)}}\right)^N \quad 4.12$$

In Table 4.1 these values are tabulated for a 1+1 (1 pass through each FP) and a 3+3 configuration (3 passes).

To scan with a single Fabry-Pérot, the mirror spacing can be changed. An other way to increase or decrease the optical wavelength in the FP is the change of the refractive index by applying pressure or heat to the medium between the two mirrors [33]. In a tandem setup with two different Fabry-Pérots the scanning is much more complicated. During a scan both maxima of the transition function have to stay always at the same relative position. This is only the case, when at all time the following condition is exactly fulfilled:

$$\frac{d_2}{d_1} = \text{const} \quad 4.13$$

For a long time, the synchronization of the movement of the two FP was nearly impossible and a scan with a tandem FP interferometer could only be performed

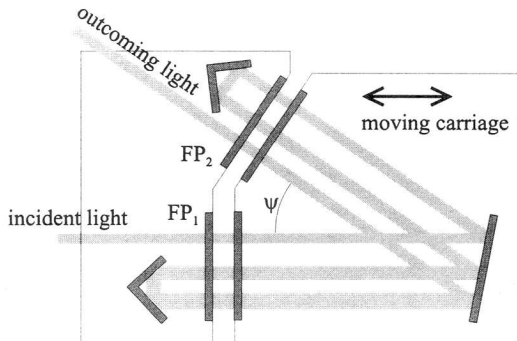


**Fig. 4.4** Principle of a 3+3 pass tandem Fabry-Pérot interferometer by Sandercock. The light passes each FP three times. The FP are mounted under an angle  $\psi$  to each other and one mirror is fixed on a movable carriage. A scan is performed by moving the carriage.

with fixed mirrors and shifting of the optical wavelength by changing the refractive index. Fortunately, John Sandercock's elegant design of placing the two Fabry-Pérots in a certain angle to each other [27], completely solved these problems (Fig. 4.4). One mirror of each FP was mounted on a carriage, that moved perpendicular to the first FP. Then the mirror spacing of the second one is automatically moved in a way that

$$\frac{d_2}{d_1} = \cos(\psi) = \text{const} \quad 4.14$$

becomes true. The big advantage of scanning by a mechanical shift is the time needed for one scan. By changing the refractive index a scan has to be performed very slowly and needs minutes or hours to be completed. On the other hand, the mechanical scan from  $-\Delta\nu$  to  $+\Delta\nu$  with a good resolution can be done within one second or less. This allows the use of electronic feedback routines to stabilize the parallelity and the spacing of the mirrors and to perform scans during hours.

In our experimental equipment a Sandercock 3+3 pass tandem Fabry-Pérot interferometer is used. The reflectivity of the mirrors is about  $R = 0.94$ , the folding angle is about  $\psi = 19^\circ$  [34]. In Table 4.1 the values of the finesse and of the contrast



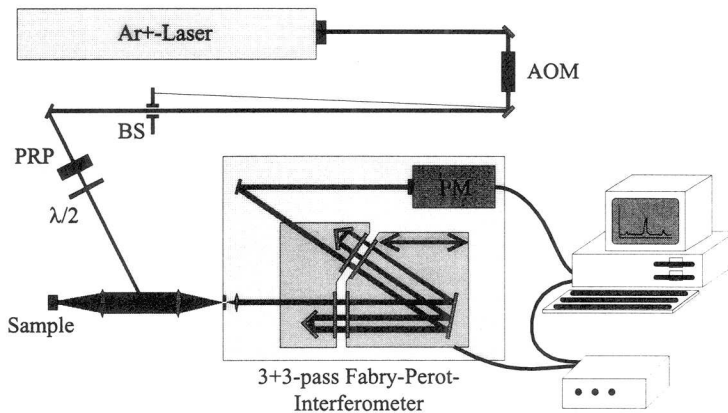


**Fig. 4.5** The experimental setup. AOM = acousto-optic modulator, BS = beam stop, PRP = polarization restoring prism,  $\lambda/2$  = phase retardation plate, PM = photo multiplier

are tabulated.

## 4.2 Experimental Setup

In Fig. 4.5 an overview of the experimental setup is shown. An Ar<sup>+</sup>-laser in single frequency mode at a wavelength  $\lambda = 514.5$  nm is used as light source. Its maximum power is about  $P \simeq 2$  W. After passing an acousto-optic modulator (AOM), a polarization restoring prism (PRP) and a phase retardation plate ( $\lambda/2$ ), the p-polarized laser beam is focused on the sample by a lens with 100 mm or 50 mm focal distance. The acousto-optic modulator is controlled by the interferometer control unit (ICU) and deflects the laser beam during programmable parts of a scan on a beam stop (BS). It is used as a fast shutter to protect the photomultiplier (PM) from overload. The degree of deflection can be adjusted. The ICU also controls the active stabilization and the scanning of the interferometer.

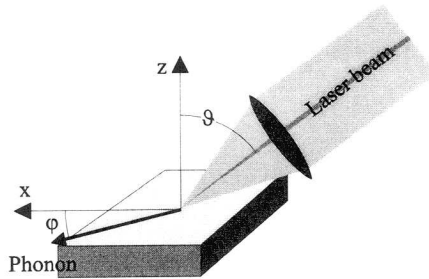


**Fig. 4.6** *The sample is mounted in a way, that the laser beam hits the sample under an incident angle  $\vartheta$ . The sample can be rotated around the z-axis ( $\varphi$ ).*

The samples are mounted on a 4 axis goniometer head, which is supported by a 6 axis holder. This allows a very precise positioning of the sample. Usually the sample is turned in a way, so that it is hit by the incident beam under an angle of  $70^\circ$  (see also chapter 3).

The scattered light is collected by the same lens as before and focused by a second lens to the entrance pin-hole of the Fabry-Pérot interferometer. The photons passing the interferometer are amplified by a photo-multiplier and counted with a high speed multichannel counter card. The analysis of the measured spectra is done by a personal computer. The free spectral range of the interferometer is usually set to 15 or 30 GHz. This corresponds to a resolution of about 0.1 to 0.2 GHz.

To avoid local hole burning on the sample the power of the incident laser is set to a value between 25 mW and 300 mW. Only about 1/3 of the light power finally hits the sample. With a focal distance of 100 mm the laser spot on the sample has a diameter of about  $20 \mu\text{m}$  [35]. Then the power density on the sample is between  $30 \text{ W/mm}^2$  and  $360 \text{ W/mm}^2$ .

Leer - Vide - Empty

# Chapter 5

## Thin film structures

As explained in chapter 2, Brillouin spectroscopy is also a good tool, to examine the elastic properties of thin films. In the following we will report of measurements on a thick PbSe film, on thin films of CoSi<sub>2</sub> in different crystallographic structures and on Fe/CoSi<sub>2</sub> superlattices. All films have been grown by molecular-beam-epitaxy on a silicon substrate with a (111) orientation of the surface. Because of the only very small surface misorientation ( $\leq 0.2^\circ$ ), the epitaxially grown films are generally extraordinary flat. This absence of nearly any disturbance on the surface decreases the amount of elastically scattered light enormously. Furthermore the reflectivity of the thin films is due to their good quality very high, which gives a high cross section for scattering on surface acoustic waves. Therefore this samples are very suitable to be examined by Brillouin spectroscopy with surface acoustic waves.

### 5.1 PbSe-layer on Si(111)

The possibility of producing IR-sensors makes the PbX (X = S, Se or Te) interesting. All PbX are semiconductors with a direct band gap at the L-point. The band gap has a positive temperature coefficient, meaning, that with increasing temperature the gap becomes larger. Good IR detectors have to be sensitive in the energy range, where the atmosphere is transparent (atmospheric windows). This is in the range of 3 - 5  $\mu\text{m}$  and 8 - 12  $\mu\text{m}$ . The gap of all PbX lies in the first window (Table 5.1). For the production of IR detectors based on PbX it is important to know also the elastic properties of this materials. The elastic constants of pure single crystals are well known [36-38], but not the one of an epitaxially grown film

	lattice constant [Å]	density $\rho$ [kg/m <sup>3</sup> ]	gap at 300K [eV]	reference
PbS	5.936	7597	0.41	[39, 41, 42]
PbSe	6.124	8276	0.27–0.29	[39, 41, 42]
PbTe	6.462	8241	0.31–0.32	[39, 41, 42]

**Table 5.1** The lattice constants, the calculated density and the band gap of PbX single crystals ( $X = S, Se, Te$ )

on a silicon substrate. In this section we want to present the measurement and the calculation we have done on PbSe films on a (111) oriented Si substrate.

PbSe has generally the simple fcc rock-salt structure. Due to the large difference of the lattice constant of PbSe (Table 5.1) and the underlying silicon ( $a = 5.430$  Å), it is not possible to grow the PbSe layer, strained with the lattice constant of the silicon, over more than one or two monolayers. During the growth process the strain energy of the layer will be minimized by building defects and dislocations into the PbSe structure. Despite this relaxation, it can not be assumed, that the whole strain vanishes. Therefore a different behavior in the elastic constants of pure PbSe and of a PbSe film on Si has to be expected.

### 5.1.1 Sample

To grow the PbSe films, first a thin template, about 20 Å thick, of CaF<sub>2</sub> was formed on the (111) oriented silicon substrate by molecular beam epitaxy (MBE). CaF<sub>2</sub> has nearly the same lattice constant as Si ( $a_{Si} = 5.430$  Å,  $a_{CaF_2} = 5.464$  Å [39]). Only this template makes it possible to grow PbSe on Si. In a second step, the PbSe layer was grown using the simultaneous electron beam evaporation of lead and selenium. With this technique PbSe films up to several micrometers can be produced. The exact method the PbSe sample was grown is described in [40].

The PbSe sample, that was used for our measurements, is about 3.5 μm thick. The lattice constant is  $a = 6.124$  Å [39].

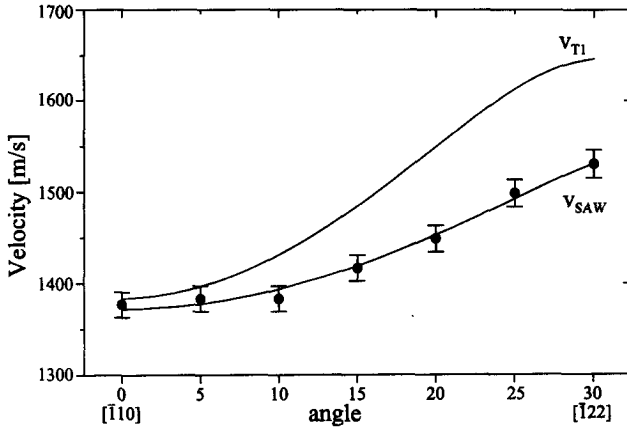


**Fig. 5.1** Angular dispersion of PbSe on Si(111). The errors are about 1%. The guidance lines denote the simulated velocities of the surface acoustic wave and a pure shear wave. The elastic constants for the simulation are calculated as described in the text.

### 5.1.2 Experimental details

Because of the thickness of the PbSe layer, the silicon substrate has hardly any influence on the velocity of the surface acoustic waves. Therefore, it makes no sense to measure a  $qd$  dispersion. Instead, the angular dispersion of  $v_{SAW}$  was measured. Thereby the incident angle was fixed at  $70^\circ$  from the plane normal and the azimuthal angle was varied between  $0^\circ$  [110] and  $30^\circ$  [122]. This range gives already all information because of the 6-fold symmetry of the (111) plane. The power of the laser was set to a maximum of 300 mW, which is equivalent to a power of about 100 mW on the sample. The free spectral range of the Fabry-Pérot interferometer was set to 15 GHz. A Brillouin spectrum was measured all  $5^\circ$  to have enough points for the following calculation. Fig. 5.1 shows the measured velocities. The errors are set to about 1%.

	$C_{11}$ [GPa]	$C_{12}$ [GPa]	$C_{44}$ [GPa]	Poisson's ratio $\nu$	Anisotropy $\eta$	Ref.
PbS	126.2	16.2	17.1	0.114	0.311	[38]
PbSe (film)	$132 \pm 10$	$61 \pm 10$	$16 \pm 5$	$0.32 \pm 0.08$	$0.45 \pm 0.27$	this work
PbSe	123.7	19.3	15.9	0.135	0.305	[37]
PbTe	108.0	7.7	13.4	0.067	0.267	[36]

**Table 5.2** *The elastic constants, Poisson's ratio and the anisotropy of single crystal PbS, PbSe and PbTe and the PbSe thin film. The large difference of elastic properties of PbSe between the values of Lippmann [37], and the one found on the epitaxially grown PbSe film, must be explained by the different preparation of the sample.*

### 5.1.3 Calculation of the elastic constants

The calculation of their elastic constants was done with the simple model of a surface acoustic wave in a semi-infinite medium. For the calculation the PbSe layer was still assumed as a pure rock-salt structure. The influence of any possible strain on the symmetry was neglected. As start value for the Levenberg-Marquard fitting algorithm the elastic constants of a pure single crystal of PbSe were used. The fitting process was applied iteratively on the measured SAW velocities to increase the accuracy of the elastic constants. In Table 5.2 the elastic properties are tabulated together with values of PbS, PbSe and PbTe single crystals, found in the literature.

### 5.1.4 Conclusions

Obviously there is quite a large difference between the values of PbSe found by Lippmann [37] and the one, determined as described before in the text. This difference can only be explained by the different way the samples have been produced. Lippmann's PbSe was a single crystal, while our sample was grown epitaxially on a Si substrate. The much higher value of  $C_{12}$  must be the result of a still present internal strain of the film structure, induced by the silicon substrate.

## 5.2 CoSi<sub>2</sub>-films on Si(111)

In the past few years, CoSi<sub>2</sub> films on Si and their synthesis have been the subject of several studies. CoSi<sub>2</sub> has in its stable phase the cubic CaF<sub>2</sub> structure with a lattice constant of  $a = 5.365 \text{ \AA}$ . At room temperature the difference to the lattice constant of the silicon is very small and a mismatch of only 1.2% occurs. Because of the thermal stability and its good electrical properties (low resistivity)[43], CoSi<sub>2</sub> is a promising candidate for application in the micro- and opto-electronics [44–46]. Besides the stable phase, there also exists a metastable phase of CoSi<sub>2</sub> with a defect CsCl structure (Fig. 5.2). To have the right stoichiometry in this phase, there are only 50% of the possible cobalt sites occupied. The vacancies are statistically distributed on the cation sites [47, 48].

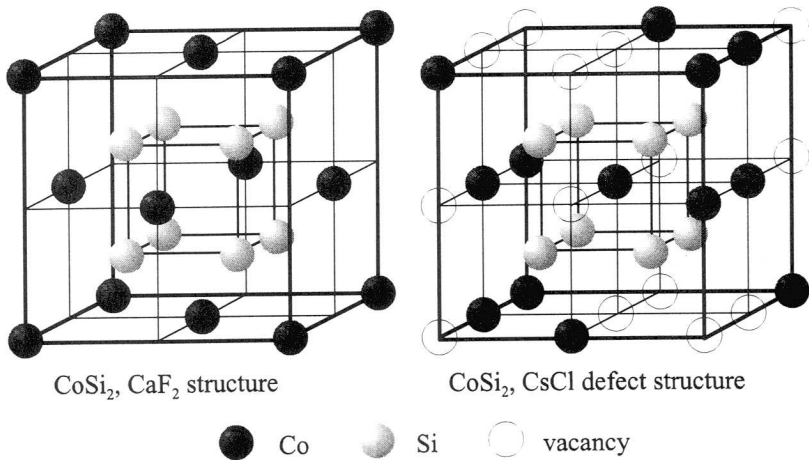


**Fig. 5.2** The left picture shows CoSi<sub>2</sub> in the well known CaF<sub>2</sub> structure. The right picture displays the new defect CsCl structure of CoSi<sub>2</sub>. In this structure only half of the cation sites are occupied by the cobalt atoms. The vacancies are distributed at random. The picture shows 8 elementary cells of the defect CsCl structure.



Structure of CoSi <sub>2</sub>	lattice constant $a$ [Å]	density $\rho$ [kg/m <sup>3</sup> ]	Poisson's ratio $\nu$
CaF <sub>2</sub>	5.365	4941	0.38
defect CsCl	2.69 ± 0.01	4773	0.33

**Table 5.3** *The lattice constants, the densities and the Poisson's ratios of both structures of CoSi<sub>2</sub>. The lattice constants and the Poisson's ratio are determined by XRD measurements as described in the text*

### 5.2.1 Samples

The silicide films were grown on a n-doped Si(111) by electron beam evaporation of Si and Co in a commercial molecular beam epitaxy (MBE) system. First a 10 Å thick template of CoSi<sub>2</sub> was formed by co-deposition of Co and Si onto the substrate. Then the template was annealed for five minutes at 420°C. Thicker films were grown onto this template by MBE with a typical deposition rate of about 1 Å/s. Finally the CoSi<sub>2</sub> was capped with a 40 Å thick silicon layer. All films, grown this way, have the metastable defect CsCl structure. To bring them into the stable CaF<sub>2</sub> structure the samples had to be annealed at 650°C for a few minutes. All films are single crystalline and have a (111) orientation of the surface. In this way samples with a thickness between about 30 and 1000 Å have been produced. The exact method, all CoSi<sub>2</sub> layers were grown, is described in details in [49–51].

The lattice constant and the strain of the film were determined by X-ray diffraction measurements (XRD). In a strained layer the lattice constant  $a$  of the relaxed structure can not be determined directly. Instead the lattice constants parallel ( $a_{\parallel}$ ) and perpendicular ( $a_{\perp}$ ) to the interface were measured. From these values the lattice constant  $a$  and Poisson's ratio were calculated [52] (see Appendix A). In Table 5.3 the lattice constant, the mass density and Poisson's ratio are tabulated.

For the Brillouin spectroscopy measurements, we used CoSi<sub>2</sub> samples with a film thickness of 100 Å, 270 Å and 1000 Å, all in both structures, the CaF<sub>2</sub> and the defect CsCl one. The two thicker samples were protected on top by a 40 Å thick silicon capping.

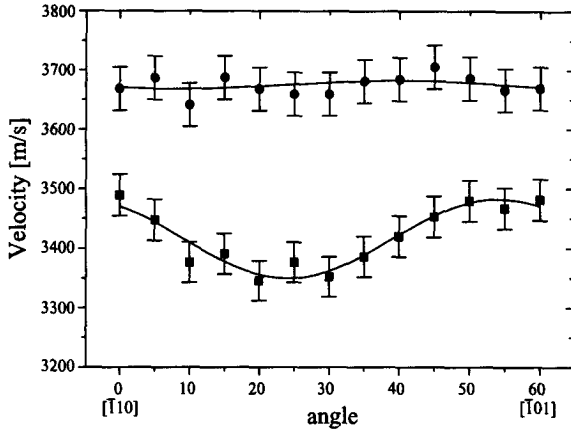


**Fig. 5.3** The angular dispersion of both structures of CoSi<sub>2</sub>, CaF<sub>2</sub> (squares) and defect CsCl (circles). The errors are 1%. The guidance lines are fitted sinus-functions to increase the visibility of the variation. The sample with the CaF<sub>2</sub> structure has a strong dependence on the angle of propagation, while the defect CsCl structure shows only a very small variation of the SAW velocities, which comes from the underlying silicon substrate.

## 5.2.2 Experimental details

In a first experiment, we measured the velocities of the surface acoustic wave in the angular dispersion of both structures. To obtain the most significant information of the film the measurements were performed on the thickest available samples (1000 Å). The laser beam hit the samples under a constant angle of 70°. The power was held at about 100 mW on the samples. The azimuthal angle was varied between 0° [ $\bar{1}10$ ] to 60° [ $\bar{1}01$ ]. Fig. 5.3 shows the angular dispersion of the CoSi<sub>2</sub> sample in the CaF<sub>2</sub> and the defect CsCl structure. While on the CoSi<sub>2</sub>(CaF<sub>2</sub>) the velocities of the surface acoustic wave vary clearly with the azimuthal angle, the sample with the CsCl structure behaves nearly isotropic and the variation of  $v_{SAW}$  lies within a range of less than 1%. Therefore we assumed the CsCl structure as isotropic. The small visible variation must be created by the underlying silicon substrate.

Since it is not possible to calculate all elastic constants of an isotropic medium

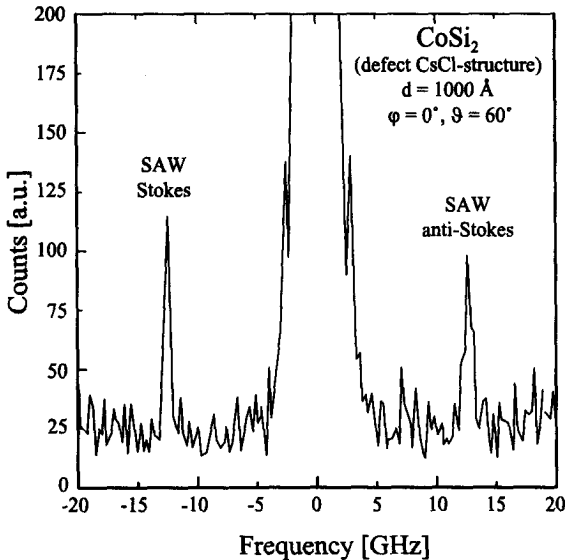


**Fig. 5.4** Typical spectrum of a  $\text{CoSi}_2$  film. Clearly visible are the sharp, needle like peaks generated by the Stokes and the anti-Stokes scattering process on surface acoustic waves. The picture shows the spectrum of the 1000 Å thick  $\text{CoSi}_2$  film with the defect CsCl structure. The direction of propagation was along  $\bar{1}10$  and the incident angle of the laser beam  $60^\circ$ .

from the angular dispersion, we also measured the dependence of  $v_{SAW}$  on  $qd$  (Chapter 2). To do so, we used all samples with both structures. Instead of varying the direction of propagation, the incident angle was moved between an angle of  $50^\circ$  and  $80^\circ$ . The direction of propagation of the SAW in the surface plane was fixed along  $\bar{1}10$ . Together with the different thickness  $d$  of the  $\text{CoSi}_2$  films the variation of the incident angle defines a  $qd$ -range from 0.18 to 2.4. Fig. 5.4 shows a typical spectrum measured on a  $\text{CoSi}_2$  film. For each film the velocity of the SAW was measured for an incident angle  $\theta = 50^\circ, 60^\circ, 70^\circ$  and  $80^\circ$ . In Fig. 5.5 all measured velocities are plotted. The errors are about 2%. Furthermore  $v_{SAW}$  of pure silicon ((111) orientation of the surface) was measured and displayed in Fig. 5.5.

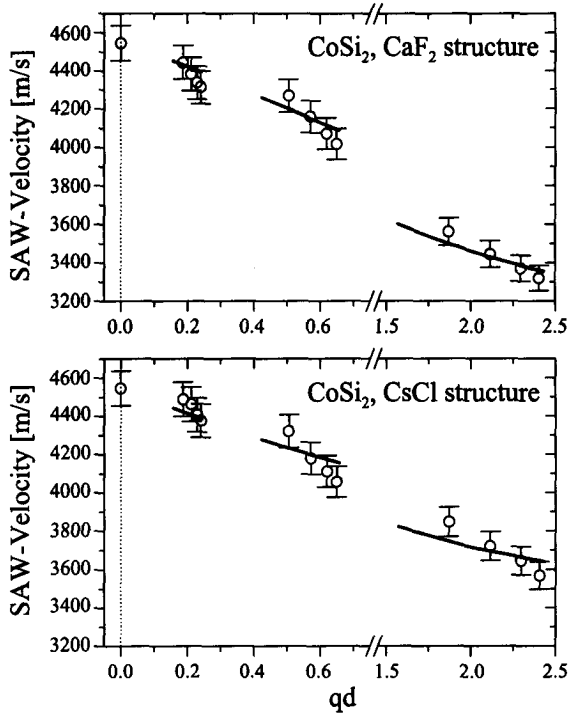


**Fig. 5.5** The  $qd$ -dispersion of CoSi<sub>2</sub>. The upper picture shows the dispersion of the known CaF<sub>2</sub> structure, the lower one displays the SAW velocities of the new defect CsCl structure. The errors are about 2%. At  $qd = 0$   $v_{SAW}$  of pure Si(111) is plotted. The full curves are generated with the use of the elastic constants, calculated as described in the text. The lines are not connected because of the different silicon capping on the CoSi<sub>2</sub> films.

### 5.2.3 Calculation of the elastic constants

To consider also the thin silicon capping on the CoSi<sub>2</sub> films, the model of a surface acoustic wave in a thin film (Chapter 2.2.6) was extended to two films. This increases the complexity of the boundary condition from a 9-dimensional problem to a 15-dimensional one (see Chapter 2.2.7). The calculations of the elastic constants were performed with the standard Levenberg-Marquard fitting algorithm [20].

First, for each sample the elastic constants were independently fitted to the measured velocities of the surface acoustic wave. As start values we used the elastic constants of  $\text{CoSi}_2$  in the  $\text{CaF}_2$  structure determined by Mendik [53], also for the samples with the defect CsCl structure. For the underlying silicon and the silicon capping on some of the samples the following values were used:  $C_{11} = 166$  GPa,  $C_{12} = 64$  GPa,  $C_{44} = 80$  GPa and the density  $\rho_{\text{Si}} = 2330$  kg/m<sup>3</sup>.

In a second step, the average elastic constants of one structure, determined as described above, were used as start value for the final calculation. Thereby, all measured velocities of one structure were considered in the fit. The resulting elastic constants are tabulated in Table 5.4. Table 5.5 shows the bulk modulus, Poisson's ratio and the anisotropy.

For the  $\text{CaF}_2$  structure  $C_{11}$  and  $C_{12}$  agree well with previously published values of the elastic constants [53–55], while for  $C_{44}$  the difference to the published values is quite large. This difference can be explained by the only weak dependence of the model function on  $C_{44}$  in the (111) plane, lowering the accuracy of this parameter in the fitting process. Poisson's ratio and the bulk modulus are also in good agreement with the already published values and also with Poisson's ratio calculated from XRD-measurements. The anisotropy shows due to the inaccurate value of  $C_{44}$  also a large difference to the published values.

For the defect CsCl structure of  $\text{CoSi}_2$  no values of the elastic constants are known. As expected from the measurements of the angular dispersion, the  $\text{CoSi}_2$  films with the defect CsCl structure show a nearly isotropic behavior. Poisson's ratio calculated from the elastic constants is also the same as the one found with the XRD measurements.

#### 5.2.4 Conclusions

To understand the isotropic behavior of the CsCl structure, one has to compare this structure with the stable  $\text{CaF}_2$  structure of  $\text{CoSi}_2$ . When looking on the two

Structure of CoSi <sub>2</sub>	$C_{11}$ [GPa]	$C_{12}$ [GPa]	$C_{44}$ [GPa]	Ref.
CaF <sub>2</sub>	227 ± 10	145 ± 10	112 ± 20	this work
CaF <sub>2</sub>	228	140	83	[54]
CaF <sub>2</sub>	240	161	74	[55]
CaF <sub>2</sub>	222	140	68	[53]
defect CsCl	260 ± 10	128 ± 10	64 ± 20	this work
Voigt's average	258 ± 26	129 ± 18	64 ± 28	this work

**Table 5.4** The elastic constants of the measured CoSi<sub>2</sub> films in both structures, CaF<sub>2</sub> and defect CsCl. Furthermore, values found in the literature and calculated from the measured values of the CaF<sub>2</sub> structure by applying Voigt's average.

Structure of CoSi <sub>2</sub>	$B$ [GPa]	Poisson's ratio $\nu$	Anisotropy $\eta$	Ref.
CaF <sub>2</sub>	172 ± 10	0.39 ± 0.04	2.75 ± 1.15	this work
CaF <sub>2</sub>	169	0.38	1.89	[54]
CaF <sub>2</sub>	187	0.40	1.87	[55]
CaF <sub>2</sub>	167	0.39	1.66	[53]
defect CsCl	172 ± 10	0.33 ± 0.04	0.96 ± 0.45	this work
Voigt's average	172 ± 20	0.33 ± 0.08	0.99 ± 0.77	this work

**Table 5.5** The bulk modulus, Poisson's ratio and the anisotropy of the measured CoSi<sub>2</sub> films in both structures, CaF<sub>2</sub> and defect CsCl. Furthermore, the values found in the literature and calculated from the measured values of the CaF<sub>2</sub> structure by applying Voigt's average.

structures in Fig. 5.2, the only differences are the sites of the cobalt atoms. While in the  $\text{CaF}_2$  structure they are placed regularly, in the defect CsCl structure they are located randomly over the whole lattice. The  $\text{CaF}_2$  structure can be regarded as one subset of all possible configurations of the cobalt ions in the defect CsCl structure. Therefore, when neglecting the Si atoms, the latter can be considered as an average of the first one. To check this possibility we calculated the elastic constants of the polycrystalline phase from the obtained data of the single crystalline  $(\text{CaF}_2)\text{CoSi}_2$  by applying the method of Voigt's average (see Appendix A). The polycrystalline phase always behaves isotropically, since all crystallographic directions are equivalent. The inaccurate value of  $C_{44}$  was replaced for the calculation by a more reliable average value of 80 GPa. In Table 5.4 and Table 5.5 the elastic properties of this average are tabulated in the row denoted Voigt's average. Obviously these values fit very nicely the results of the measurements on the defect CsCl structure. This calculation explains also the agreement of the bulk modulus obtained in both different structures, since the bulk modulus is invariant under the phase transition from the single crystalline phase to the polycrystalline one.

The calculation shows also, that the silicon lattice in the structure can only have a very small influence on the elastic behavior of the  $\text{CoSi}_2$  films.

### 5.3 CoSi<sub>2</sub>/Fe superlattices on Si(111)

Besides the single crystalline CoSi<sub>2</sub> films on a silicon substrate, it is also possible to grow superlattices with CoSi<sub>2</sub> and Fe. Thereby the CoSi<sub>2</sub> is in the defect CsCl structure. The iron is formed in very thin layers (only one or two monolayers). In a superlattice two or more different materials are periodically repeated with always the same layer thickness. The interest in such superlattices comes from the search of materials with new properties. In this case, the CoSi<sub>2</sub>/Fe superlattices are interesting because of the 2-dimensional iron layers, which might be still magnetic. In fact, measurements of the electrical properties showed an anomalous Hall effect on CoSi<sub>2</sub>/Fe superlattices and therefore, give the possibility to be a ferro- or an antiferromagnet [56, 57]. But it was not possible to verify this effect by Brillouin scattering experiments on Damon-Eshbach modes [53]. Nevertheless, we performed Brillouin spectroscopy on these superlattices to determine the elastic constants of these superlattice films.

#### 5.3.1 Samples

In a MBE system, first a thin CoSi<sub>2</sub> template in the CaF<sub>2</sub> structure (30 Å) was formed on a (111) oriented, n-doped silicon substrate by co-deposition of Si and Co (see section 5.2.1 of this chapter) [56]. Then, periodically, the layers of Fe and of CoSi<sub>2</sub>(CsCl) were grown to produce the superlattice. The exact method,

Sample	thickness Fe [Å]	thickness CoSi <sub>2</sub> [Å]	periods	thickness film [Å]	density $\rho$ [kg/m <sup>3</sup> ]
8016	3.0	21	10	240	5159
8017	1.5	14	22	341	5072
8022	1.5	3.5	30	150	5699

**Table 5.6** Thickness of the iron and CoSi<sub>2</sub> layers, number of periods, total thickness and average density of the CoSi<sub>2</sub>/Fe superlattices



the superlattices were grown, is described in details in [51, 56]. Table 5.6 shows the properties of the investigated  $\text{CoSi}_2/\text{Fe}$  superlattice samples. The densities of the superlattice films were calculated as the average of the densities of pure iron ( $\rho_{\text{Fe}} = 7860 \text{ kg/m}^3$ ) and of  $\text{CoSi}_2$  in the defect CsCl structure ( $\rho_{\text{CoSi}_2} = 4773 \text{ kg/m}^3$ ), weighted by the thickness of the single layers. In the first sample (8016) the thickness of the iron is equivalent to about two monolayers, in the other two systems to about one monolayer. Because of a possible dispersion of Si atoms, the exact structure of the iron layer is not known. Besides the pure Fe with a bcc structure, it can also be  $\text{Fe}_3\text{Si}$ ,  $\text{FeSi}$  or  $\text{FeSi}_2$  [48]. At the moment no further characterization of the structures are available.

### 5.3.2 Experimental details

Because of the thicker superlattice structure, the  $qd$  dispersion was measured, on the first two samples (8016 and 8017). The direction of propagation was always fixed along the crystallographic [100] direction. The power of the laser was held at about 100 mW on the sample and the free spectral range was set to 30 GHz. The incident angle of the laser beam was varied between  $45^\circ$  and  $80^\circ$ , which is equivalent to a variation of  $qd$  between 0.4 and 0.6 for the thinner sample (8016) and between 0.55 and 0.85 for the thicker one (8017). Fig. 5.6 shows all measured velocities of the surface acoustic waves for both samples. The error of the measurements was about 1%.

On the thinnest sample of the  $\text{CoSi}_2/\text{Fe}$  superlattices (8022) the angular dispersion was measured. Thereby the incident angle was fixed at  $70^\circ$  from the plane normal and the azimuthal angle was varied, due to the 6-fold symmetry of the (111) plane, from  $0^\circ$  ( $\bar{1}10$ ) to  $30^\circ$  ( $\bar{1}22$ ). As before the power was held at about 100 mW on the sample and the free spectral range was set to 30 GHz. All  $5^\circ$  a spectrum was measured. Fig. 5.7 shows the measured angular dispersion of the  $\text{CoSi}_2/\text{Fe}$  superlattice (8022). The plotted errors are 1%, except at  $30^\circ$  ( $\bar{1}22$ ), where it is 2%.

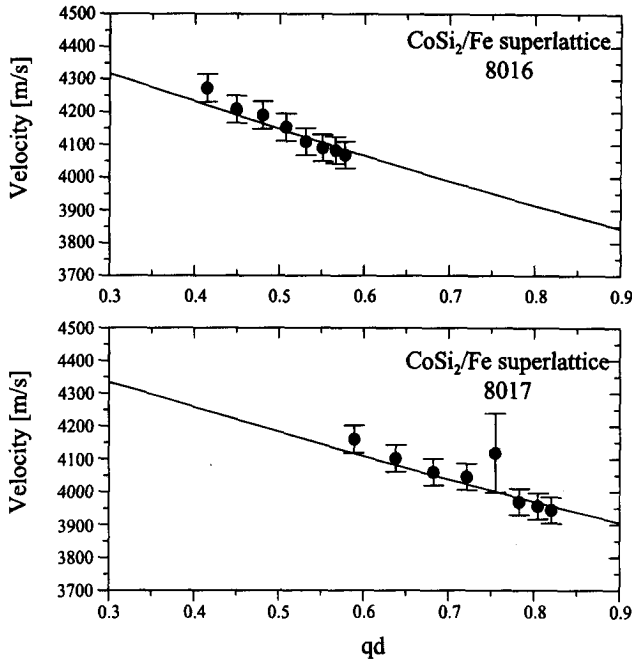


**Fig. 5.6**  $qd$ -dispersion of the  $\text{CoSi}_2/\text{Fe}$  superlattice (sample 8016 and 8017). The plotted errors are about 1%. The guidance lines are simulated using the elastic constants of the superlattices, calculated as described in the text.

### 5.3.3 Calculation of the elastic constants

For the calculation of the elastic constants the model of a surface acoustic wave in a thin film was used. Thereby, it was the goal to determine the elastic constants of the total superlattice and not of a single layer. Therefore the superlattice was assumed as a film of one homogeneous material. No distinction between the different layers was made. For the mass density the weighted average of the densities of the different layer materials was taken as described in the previous section (5.3.1). For the underlying silicon substrate, the elastic constants were taken from the literature [10]:  $C_{11} = 166$  GPa,  $C_{12} = 64$  GPa,  $C_{44} = 80$  GPa and the mass density  $\rho_{\text{Si}} = 2330$

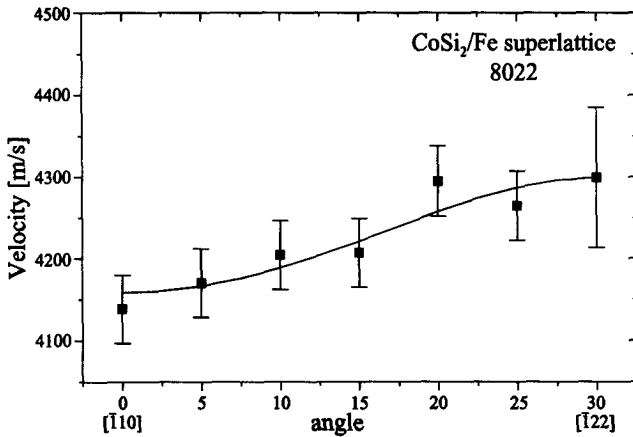


Fig. 5.7 Angular dispersion of  $\text{CoSi}_2/\text{Fe}$  superlattice (sample 8022). The errors are about 1% (except at  $30^\circ$ , where it is 2%). The guidance line is a simulation using the elastic constants of the superlattice, calculated as described in the text.

Sample	$C_{11}$ [GPa]	$C_{12}$ [GPa]	$C_{44}$ [GPa]	$B$ [GPa]	Poisson's ratio $\nu$	Anisotropy $\eta$
$\text{CoSi}_2$	$260 \pm 10$	$128 \pm 10$	$64 \pm 20$	$172 \pm 10$	$0.33 \pm 0.04$	$0.96 \pm 0.45$
8016	$232 \pm 10$	$155 \pm 10$	$94 \pm 10$	$181 \pm 10$	$0.40 \pm 0.05$	$2.44 \pm 0.89$
8017	$261 \pm 10$	$175 \pm 10$	$88 \pm 10$	$204 \pm 10$	$0.40 \pm 0.04$	$2.05 \pm 0.71$
8022	$225 \pm 10$	$151 \pm 10$	$52 \pm 10$	$176 \pm 10$	$0.40 \pm 0.05$	$1.41 \pm 0.65$
Fe	243	138	121	173	0.49	2.32

Table 5.7 The elastic constants, the bulk modulus, Poisson's ratio and the anisotropy of the  $\text{CoSi}_2/\text{Fe}$  superlattices. The errors are estimated from the inaccuracy of the measurement and the fitting process

$\text{kg/m}^3$ .

As starting values for the first calculated sample (8016), the values of the elastic constants of pure  $\text{CoSi}_2$  in the defect CsCl structure were used. For the other samples, starting values were set to the calculated values of the  $\text{CoSi}_2/\text{Fe}$  superlattice sample 8016. As before the standard Levenberg-Marquard algorithm was used for the fitting. To improve the accuracy it was applied iteratively to the measured

---

values of the SAW velocities. Table 5.7 shows the elastic constants of the  $\text{CoSi}_2/\text{Fe}$  superlattices, their bulk modulus, Poisson's ratio and their anisotropy. The errors are estimated from the inaccuracy of the measurements and of the calculations.

While Poisson's ratios of all measured superlattice samples are exactly the same, the other elastic properties differ a lot. Specially the anisotropy varies in a very wide range.

### 5.3.4 Conclusions

Obviously, the elastic properties of these structures depend very much on the exact parameters of the superlattice. From X-ray measurements one can conclude, that in the sample with the 3 Å iron period (8016) and also in the sample with the only 3.5 Å thin  $\text{CoSi}_2$  films (8022) the iron layers are relaxed. Table 5.7 shows, that  $C_{11}$ ,  $C_{12}$  and  $B$  are very similar for these two superlattice structures. On the other hand, in the sample consisting of a superlattice with 1.5 Å thick Fe and 14 Å thick  $\text{CoSi}_2$  (8017), the iron layers are not relaxed, but still strained with the lattice constant of the  $\text{CoSi}_2$  in the defect CsCl structure. May be this explains the difference in the elastic constants to the other samples.

The reason for the wide variation of  $C_{44}$  and therefore, of the anisotropy is not very clear. Astonishing is the large value for the anisotropy in the two samples with thick  $\text{CoSi}_2$  layers (8016 and 8017), while pure  $\text{CoSi}_2$  in the defect CsCl structure behaves isotropically. On the other side, in the sample with only very thin  $\text{CoSi}_2$  films, the anisotropy tends to one. Therefore one has to assume, that the iron film is not in its pure bcc phase, but in a silicide form like  $\text{Fe}_3\text{Si}$ ,  $\text{FeSi}$  or  $\text{FeSi}_2$ .

Leer - Vide - Empty

# Chapter 6

## Elastic properties of doped SmS

### 6.1 Introduction

SmS is a semiconductor, at normal pressure and room temperature, with a gap of about 200 meV between the  $4f^6$  state and the  $5d$  band [58]. It is well known that at an applied pressure of about 6.5 kbar (= 650 MPa) SmS becomes *intermediate valent*

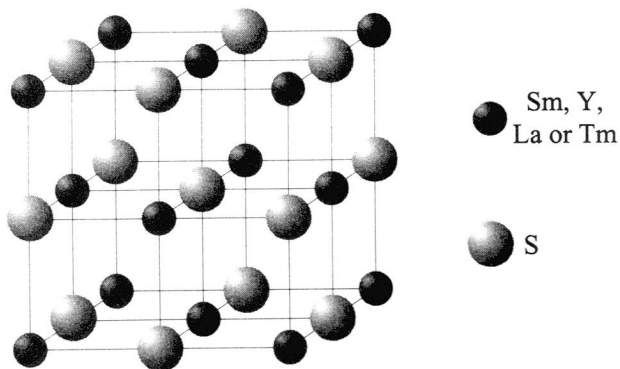
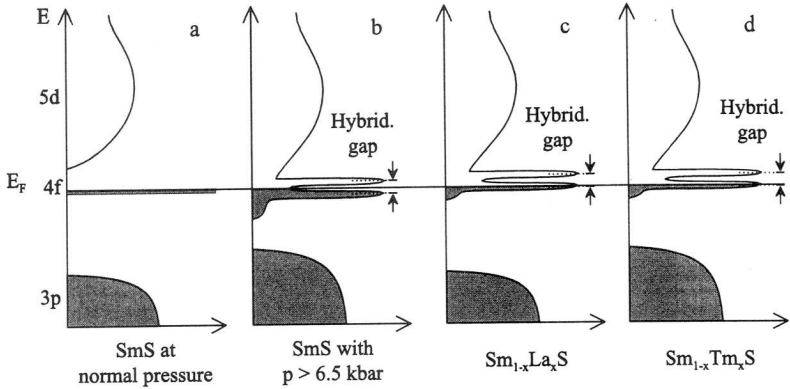


Fig. 6.1 Rocksalt structure of SmS, where the Sm ions can be substituted by Y, La or Tm atoms.

and shows a metallic behavior [59]. Thereby, the pressure induced broadening of the  $5d$  band creates an overlap between the  $4f$  state and the  $5d$  band. As a consequence of the overlap the  $4f^6$  state and the  $4f^55d^1$  state hybridize. Therefore, a  $4f$  electron has also a  $5d$  electron character. The mixing of the character of the electron leads to the broken valence number. This effect is called *intermediate valence*. The hybridization creates additionally a new small pseudo gap (hybridization gap) of about  $\Delta E = 6.4$  meV between the mixed  $4f^6 - 4f^55d^1$  states [60]. The Fermi energy  $E_F$  is always pinned somewhere in this gap (Fig. 6.2a,b).

Besides an applied external pressure, the substitution of the divalent Sm ion by another trivalent cation can also create the necessary overlap between the  $4f$  and the  $5d$  state and bring the SmS compound in the intermediate valent state. Thereby two mechanisms are possible: In the first case, the substituting cation has clearly a smaller ionic radius than  $\text{Sm}^{2+}$ . Then, the rocksalt structure (Fig. 6.1) is set under an internal chemical pressure which broadens the  $5d$  band [61]. On the other hand, as pointed out by Falicov, Kimball [62] and Robinson [63], it is enough to substitute Sm by a trivalent ion like La to make the SmS compound intermediate valent. A smaller ionic radius is then not necessary. Trivalent La has only a slightly smaller ionic radius than divalent Sm and therefore, creates hardly a lattice pressure. In this second mechanism, the main effect leading to intermediate valence is the existence of one free electron pro La atom in the conduction  $5d$  band. These electrons are able to shield very effectively the positive charge left behind by an electron, that moves from the localized  $4f$  state into the  $5d$  band, and decrease in this way the binding energy of the  $4f$  electrons. In other words, the  $4f$  state is lifted up relatively to the  $5d$  band and creates in this way the necessary overlap between the two states. Of course, both mechanism can contribute simultaneously to the intermediate valent behavior of doped SmS as e.g. in Y doped SmS.

Strong evidence of intermediate valence is a negative value of Poisson's ratio (Eq. 2.16) [5–7]. Generally Poisson's ratio describes the degree of conservation of the volume, when applying an uniaxial pressure. A value of 0.5 expresses a total conservation of the volume, while a negative value of Poisson's ratio describes a



**Fig. 6.2** a) shows the electronic configuration of SmS at normal conditions. When applying a pressure all electron bands broaden. At a pressure of about 6.5 kbar the broadening of the 5d band is strong enough to overlap and to hybridize with the 4f state (b). On the other hand, when substituting samarium with the trivalent lanthanum with its only minutely smaller ionic radius, it is not a broadening of the 5d band, that leads to intermediate valence, but a lifting of the 4f state due to a decrease of the binding energy (c). Because of the clearly smaller ionic radius of Tm than of Sm, the mechanism leading to intermediate valency in  $\text{Sm}_{1-x}\text{Tm}_x\text{S}$  must be a mixture of both, the chemical pressure and the decreased binding energy at the same time.

collapsing of the volume. In the case of intermediate valent materials the typical collapsing of the lattice constant during the semiconductor-metal transition [61] leads to a negative value of Poisson's ratio. The origin of the collapse can be found in the special electronic configuration of intermediate valent materials and can be explained by the different character of the 4f and the 5d electron states.

Whereas the 4f electrons are strongly localized quite near the atomic nucleus, the 5d states are located much more on the periphery of the atom. If an electron is taken from a 4f state and put into a 5d state, the remaining  $4f^{n-1}$  electrons screen less effectively the positive charge of the nucleus. Therefore, the outer electrons are attracted by a stronger Coulomb force and the whole electronic hull shrinks a bit. Generally this process needs some energy to overcome the energy-gap between the two involved states (4f and 5d). But in an intermediate valent system, these two



states overlap and mix already. That's why a  $4f$  electron is able to change its state without the use of any energy. Already a small pressure or density fluctuations are then enough to increase the probability for a  $4f$  electron to be in a  $5d$  state and to provoke the isotropic collapse of the crystal.

To have a negative value of Poisson's ratio either  $C_{11}$  or  $C_{12}$  must be negative. From the condition of a positive definite strain energy (Eq. 2.11) it follows immediately, that in a cubic material only  $C_{12}$  can be negative.

In the following sections measurements on La and Tm doped SmS and the calculation of their elastic constants are presented.

## 6.2 La doped SmS

The doping of SmS with La is very interesting because on these compounds it can be clearly shown, that free electrons play an important part in the intermediate valence of SmS. An internal chemical pressure is not necessary. Lanthanum is always trivalent and has only a minutely smaller ionic radius than the divalent Sm. Therefore, built in La can hardly set the rocksalt structure of SmS under an adequate, chemical pressure. Nevertheless, its intermediate valence has been already proved by Holtzberg [64] and Wachter [65]. A clear evidence for the importance of the Falicov-Kimball-model [62] is given by the lattice constants (Table 6.1). The lattice constant of intermediate valent, La doped SmS can become smaller than the lattice constant of pure LaS. But in such a case the La can not produce any lattice pressure. The intermediate valence must be only the effect of the free electrons of the La in the conduction  $5d$  band. Furthermore, Wachter et al. [58,65] showed, that  $\text{Sm}_{0.75}\text{La}_{0.25}\text{S}$  under pressure is the second excitonic insulator beside  $\text{TmSe}_{1-x}\text{Te}_x$ , which was found first by Neuenschwander and Wachter [66] and confirmed by Bucher et al. [67]. On the other hand, on Y doped SmS, due to its higher concentration of free electrons, the behavior of an excitonic insulator was never found [68].

	lattice constant $a$ [Å]	density $\rho$ [kg/m <sup>3</sup> ]
SmS	5.966	5706
Sm <sub>0.90</sub> La <sub>0.10</sub> S	5.934	5761
Sm <sub>0.75</sub> La <sub>0.25</sub> S	5.866	5911
Sm <sub>0.65</sub> La <sub>0.35</sub> S	5.846	5908
LaS	5.857	5652

**Table 6.1** Lattice constants of  $Sm_{1-x}La_xS$  measured by X-ray powder diffraction and the mass density of the measured single crystals. The error of the lattice constants is about  $\pm 0.001$

### 6.2.1 Samples

The exact method to grow the La doped Sm samples is described in details in [69]. At first all elements were put in the right stoichiometric ratio in a vacuum tight quartz tube. This work was done in a glove box. Then, the tube was heated up very slowly – over a period of two or three weeks – to a temperature of 600-800°C, where the reaction took place. Afterwards the micro crystalline products were molten in a closed tungsten crucible at about 2000°C and then in a small temperature gradient the large single crystals were grown.

In this way single crystalline  $Sm_{1-x}La_xS$  with a La concentration of  $x = 10\%$ ,  $25\%$  and  $35\%$  have been grown. At normal pressure all samples have a dark color (dark violet to black). For the measurements, crystals with an edge length of approximately 2-5 mm were used. The single crystals were cleaved along the (100) planes. In spite of the cleaved surface, the surface was still microscopically very rough and, moreover, the samples were very sensitive against excessive heating. To increase the reflectivity and the thermal conductivity of all three crystals a very thin gold film was sputtered on them. The thickness of the film was about 100 Å. Besides the increased reflectivity and thermal conductivity the thin layer protects the SmS compound also against the reaction with the humidity of the environment.

Thanks to the RF-sputtering, the quality of the thin films is very good and they can be considered as homogeneous. Generally sputtered gold films grow with a strong [111] texture along the growing direction but with random orientation of

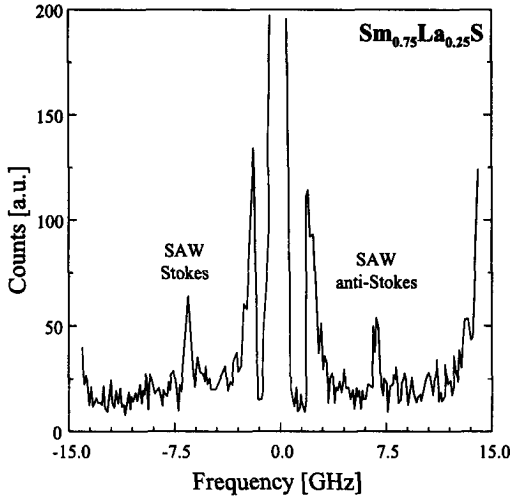


**Fig. 6.3** The measured spectrum of  $\text{Sm}_{0.75}\text{La}_{0.25}\text{S}$ . The incident angle of the laser beam was  $\Theta = 70^\circ$  and the direction of propagation along  $[100]$ . Clearly visible are the peaks created by the Stokes and the anti-Stokes scattering process. The two sharp peaks in the middle belong to the flanks of the elastically scattered light.

the film parallel to the plane. Because of the very small thickness of the film, its influence on a surface acoustic wave is small. Furthermore, the differences of the elastic constants of gold in the effective  $D_{6h}$  and in an assumed isotropic symmetry are small, as well. Therefore, we assumed the gold layer for the calculations as fully polycrystalline and isotropic.

The lattice constants of all measured La doped SmS compounds were measured by a X-ray powder diffraction-method in transmission mode (STOE powder diffractometer). Thereby the samples were ground to powder. Because of a possible phase transition of the  $\text{Sm}_{1-x}\text{La}_x\text{S}$  under pressure, it is not obvious, that the powder has the same lattice constant as the single crystals. But, as it will be shown in section 6.3, the powder diffraction method is very reliable and the differences are within the error of the measurements.

The lattice constants are tabulated together with the densities in Table 6.1.

### 6.2.2 Experimental details

All samples were hit by the laser beam under an angle of  $70^\circ$ . The power of the laser on the single crystals was held below a maximum of 35 mW to avoid local hole burning. The free spectral range (see Chapter 4) was set to 15 GHz. All experiments were performed at room temperature. For a typical spectrum of  $\text{Sm}_{1-x}\text{La}_x\text{S}$  (Fig. 6.3) about 15000 scans of the Fabry-Pérot were done with the use of 256 channels. The total sampling time was about 1.5–2 hours. The two sharp peaks are generated by the Stokes and the anti-Stokes process on a surface acoustic wave propagating on the (001) plane. As a consequence of the metallic behavior of the La doped SmS and the additional gold film, with its high reflectivity, the light of the laser gets absorbed very quickly and can only penetrate  $\sim 500 \text{ \AA}$  into the sample. Therefore the scattering volume is so small that scattering on bulk phonons can be neglected. The scattering on surface acoustic waves takes place just on ripples of the surface. Nevertheless the surface acoustic waves have a penetration depth of several  $\mu\text{m}$  and probe the bulk of the SmS samples in a good manner (see Chapter 2 and 3).

For all three doping concentrations, spectra at five different azimuthal angles were taken:  $\varphi = 0^\circ[100], 10^\circ, 20^\circ, 35^\circ$  and  $45^\circ[110]$  (Fig. 6.4).

### 6.2.3 Calculation of the elastic constants

For each sample the elastic constants were calculated. In a first step the thin gold film was neglected and the model of a simple surface acoustic wave in a semi infinite material (section 2.2.5) was used to do a rough calculation of the  $C_{IJ}$ . Because of the expected *quasi-isotropic* behavior (anisotropy  $\eta < 1$  (Eq. 2.17), see Fig. 2.9), the  $v_{SAW}$  was only about 1-10% smaller than the constant shear velocity  $v_{T_1}$  (Eq. 2.22) over the whole angular dispersion relation, from [100] to [110]. Therefore the start value of  $C_{44}$  could be guessed very well. The start values of  $C_{11}$  and  $C_{12}$  were obtained from published values of similar materials (e.g.  $\text{Sm}_{0.75}\text{Y}_{0.25}\text{S}$  presented by

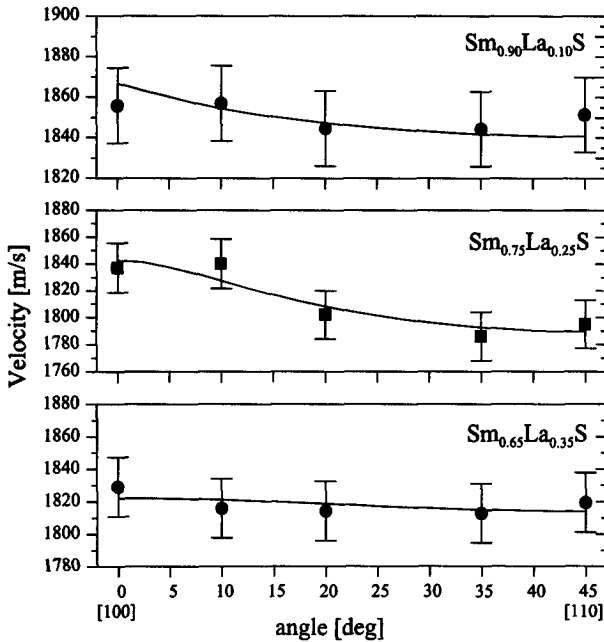


Fig. 6.4 Angular dispersion of the SAW in the (100)-plane of  $\text{Sm}_{1-x}\text{La}_x\text{S}$  with  $x = 0.90, 0.75$  and  $0.65$ . The errors are all about 1%. The lines are generated using the elastic constants calculated as described in the text.

Zirngiebl and Güntherodt [70]). To get the elastic constants, these start values were used to perform a least-square fit by the standard Levenberg-Marquard algorithm [20].

To consider the thin gold film and to improve the calculations, the model of a SAW in a thin film (section 2.2.6) was used. As mentioned above the gold layer was assumed as polycrystalline and isotropic. The elastic constants of gold were calculated from the elastic constants of single crystalline gold by using the method of Voigt's average (see Appendix A). The elastic constants are then:  $C_{11} = 220.2$  GPa,  $C_{12} = 160.4$  GPa and  $C_{44} = 29.9$  GPa and the mass density:  $\rho = 19493$  kg/m<sup>3</sup>.

During the fitting it turned out, that  $C_{11}$  and  $C_{12}$  are strongly coupled and that

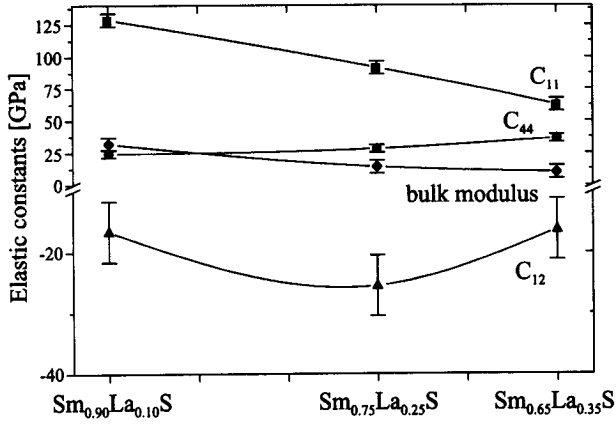


Fig. 6.5 Calculated elastic constants and measured bulk modulus of  $\text{Sm}_{1-x}\text{La}_x\text{S}$  depending on the doping concentration of La

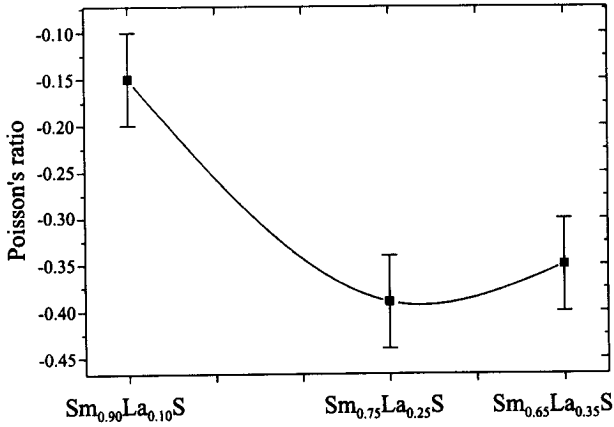


Fig. 6.6 Calculated Poisson's ratios of  $\text{Sm}_{1-x}\text{La}_x\text{S}$  depending on the doping concentration of La.

	$C_{11}$ [GPa]	$C_{12}$ [GPa]	$C_{44}$ [GPa]	Bulk modulus $B$ [GPa]	Poisson's ratio $\nu$
$\text{Sm}_{0.90}\text{La}_{0.10}\text{S}$	$128 \pm 5$	$-17 \pm 5$	$24 \pm 3$	$32 \pm 5$	$-0.15 \pm 0.06$
$\text{Sm}_{0.75}\text{La}_{0.25}\text{S}$	$91 \pm 5$	$-26 \pm 5$	$28 \pm 3$	$14 \pm 5$	$-0.40 \pm 0.14$
$\text{Sm}_{0.65}\text{La}_{0.35}\text{S}$	$62 \pm 5$	$-16 \pm 5$	$36 \pm 3$	$10 \pm 5$	$-0.35 \pm 0.18$

**Table 6.2** The calculated elastic constants, the measured bulk modulus and the Poisson's ratio of  $\text{Sm}_{1-x}\text{La}_x\text{S}$ .

they can compensate each other. Reliable results can be obtained by fixing these elastic constants together with the bulk modulus  $B$  (Eq. 2.15). The bulk modulus was measured by volume-pressure experiments by Jung et al. [71].

To increase the accuracy, the fitting process was used iteratively. The calculated elastic constants together with Poisson's ratios and the measured bulk moduli are tabulated in Table 6.2. The errors were estimated by the measurement error and the inaccuracy of the fit.  $C_{11}$ ,  $C_{44}$  and the bulk modulus, shown in Fig. 6.5, are characterized by a monotonous, nearly linear dependence on the doping level, whereas  $C_{12}$  is negative and has a clear minimum near the SmS compound doped with 25% La. The fact of a negative  $C_{12}$  leads also to a negative value of Poisson's ratio in  $\langle 100 \rangle$ -direction (Fig. 6.6).

## 6.2.4 Calculation of the valence

Using the measured lattice constants we calculated also the valence of  $\text{Sm}_{1-x}\text{La}_x\text{S}$ . To do so, we supposed a hybridization between  $\text{Sm}^{2+}$  and  $\text{Sm}^{3+}$  ( $4f^6 - 4f^5 5d^1$ ) cations. Furthermore we assumed that the ionic radii of the cations and anions can simply be summed up. Then the lattice constant  $a$  can be expressed, using Vegard's law, as:

$$a_{\text{Sm}_{1-x}\text{La}_x\text{S}} = 2 \cdot \{ \{ y \cdot r_{\text{Sm}^{2+}} + (1 - y) \cdot r_{\text{Sm}^{3+}} \} \cdot (1 - x) + x \cdot r_{\text{La}^{3+}} + r_{\text{S}^{2-}} \} \quad 6.1$$

where  $y$  describes the ratio of  $\text{Sm}^{2+}$ . The factor 2 comes from the rocksalt structure.

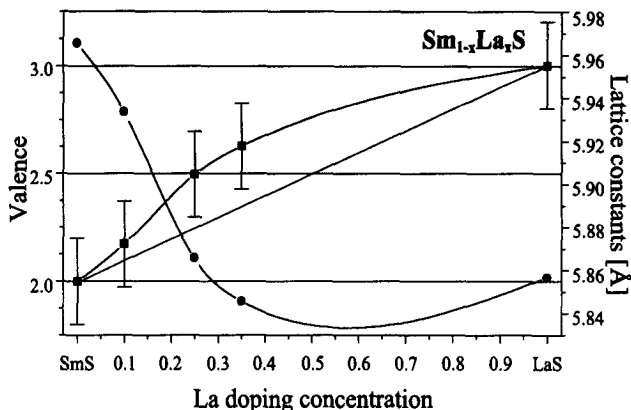


Fig. 6.7 Doping dependence of the valence (squares) and of the lattice constant (circles) of  $\text{Sm}_{1-x}\text{La}_x\text{S}$ . At a La concentration of about 25% the valence shows the largest divergence from the linear behavior.

The radii of  $\text{Sm}^{2+}$  ( $= 1.143 \text{ \AA}$ ) and of  $\text{La}^{3+}$  ( $= 1.089 \text{ \AA}$ ) were calculated from the lattice constant of pure SmS and  $\text{LaS}^2$ . The values of  $\text{Sm}^{3+}$  ( $= 0.964 \text{ \AA}$ ) and  $\text{S}^{2-}$  ( $= 1.84 \text{ \AA}$ ) were taken from literature [72]. Using the fraction  $y$  from Eq. 6.1 the valence of the samarium can be calculated by:

$$v_{\text{Sm}} = 3 - y \quad 6.2$$

and the total valence of the compound by:

$$v_{\text{Sm}_{1-x}\text{La}_x\text{S}} = 3 - y \cdot x \quad 6.3$$

In Fig. 6.7 the valence of  $\text{Sm}_{1-x}\text{La}_x\text{S}$  and the measured lattice constants are plotted versus the La-doping concentration. Moreover, we calculated the valence of  $\text{Sm}_{1-x}\text{La}_x\text{S}$  using the bond-valence-model [73]. The results obtained by this method are in a very good agreement with the valences calculated by using Vegard's law.

As it can be seen, the increase of the valence is clearly stronger than expected from

<sup>2</sup> The ionic radius of  $\text{La}^{3+}$  is not very well determined. E.g. in the periodic table of the elements by Sargent-Welch a value of  $1.15 \text{ \AA}$  is given. But also much smaller values can be found in the literature.



the increase of the concentration, e.g. for  $\text{Sm}_{0.75}\text{La}_{0.25}\text{S}$  the valence is 2.5 instead of 2.25 (linear approximation). At a La concentration of about 25 % the valence has the largest difference to the linear behavior. This is also in a very good agreement with the measurement of the elastic constants and of Poisson's ratio, where around the same doping concentration the largest negative values have been found (Table 6.2).

## 6.3 Tm doped SmS

In contrast to the always trivalent lanthanum, Tm changes its valence, when built in SmS. Pure TmS is a metal and in this state the thulium ion is trivalent, whereas in only weakly doped SmS it is divalent. Following Smirnov et al. [74, 75] (see also Fig. 6.8) three different doping ranges can be distinguished. From a doping concentration of 0% to about 16% both cations are divalent. Then, Tm changes its valence rapidly to 3, whereas the samarium stays in the divalent state. At a concentration level of 25% the Sm also begins to change its valence from 2 to 3. In contrast to the valence change of the thulium, this change is less abrupt and goes over the whole range from 25% to 100%.

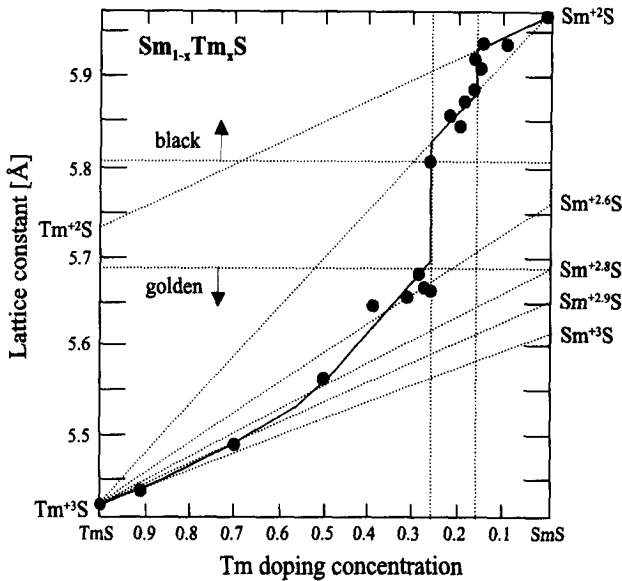


Fig. 6.8 The lattice constants and the valencies of  $\text{Sm}_{1-x}\text{Tm}_x\text{S}$  depending on the Tm doping concentration measured by Smirnov et al. [74]. Clearly visible are the steps in the lattice constant. From a Tm concentration of about 25% the color of the compounds changes from black to golden.

Compared with the ionic radius of  $\text{La}^{3+}$  ( $= 1.089 \text{ \AA}$ ) and of  $\text{Sm}^{2+}$  ( $= 1.143 \text{ \AA}$ ), the radius of  $\text{Tm}^{3+}$  is clearly smaller and only  $0.87 \text{ \AA}$ . Therefore, the intermediate valence of  $\text{Sm}_{1-x}\text{La}_x\text{S}$  must be also the result of an internal chemical pressure, besides the screening effect of the free electrons. Thereby not only the binding energy of the  $4f$  electrons is decreased, but also the  $5d$  band broadens (Fig. 6.2).

### 6.3.1 Samples

The  $\text{Sm}_{1-x}\text{Tm}_x\text{S}$  samples were produced with the same method as described in section 6.2.1. In this way single crystalline  $\text{Sm}_{1-x}\text{Tm}_x\text{S}$  with a thulium concentration of  $x = 10\%$ ,  $15\%$  and  $25\%$  have been grown. For the measurements crystals with an edge length of about 3-5 mm were used. The single crystals have been also cleaved along the (100) plane.

Generally the Tm doped SmS compounds are, like the La doped ones, very sensitive against excessive heating and the cleaved surfaces are still very rough. Therefore, we also sputtered a thin gold film of  $100 \text{ \AA}$  with the RF-sputter technique on the 10% and 15% Tm doped compounds to increase the thermal conductivity and the reflectivity. In contrast to these weakly doped samples with their dark color,  $\text{Sm}_{0.75}\text{Tm}_{0.25}\text{S}$  has a golden color, making not necessary any enhancement of the thermal conductivity and of the reflectivity. Because a gold film also protects the crystal surface against the reaction with the humidity of the environment, the unlayered  $\text{Sm}_{0.75}\text{Tm}_{0.25}\text{S}$  had to be investigated in a He atmosphere.

The lattice constants of all Tm doped SmS compounds were determined by a X-ray powder diffraction-method in transmission mode. To do so, it was necessary to grind the crystals to powder. Because of the possible phase change of pure and doped SmS under pressure, the reliability of the method was checked by measuring also a  $\text{Sm}_{0.90}\text{Tm}_{0.10}\text{S}$  single crystal in a reflection mode. This experiment gave, within the error of the measurements, the same result of lattice constant for the 10% doped SmS compound. In a third experiment the surface of a  $\text{Sm}_{0.90}\text{Tm}_{0.10}\text{S}$

	lattice constant $a$ [Å]	density $\rho$ [kg/m <sup>3</sup> ]
SmS	5.966	5706
Sm <sub>0.90</sub> Tm <sub>0.10</sub> S	5.905	5946
Sm <sub>0.85</sub> Tm <sub>0.15</sub> S	5.860	6114
Sm <sub>0.75</sub> Tm <sub>0.25</sub> S	5.682	6772

**Table 6.3** Lattice constants of Sm<sub>1-x</sub>Tm<sub>x</sub>S measured by X-ray powder diffraction and the mass density of the measured single crystals. The error of the lattice constants is about  $\pm 0.001$

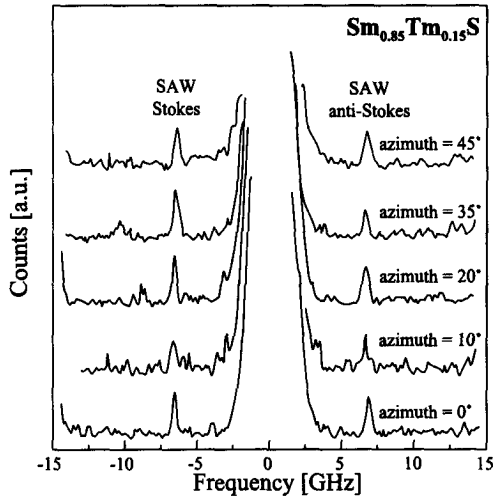


**Fig. 6.9** The measured spectra of Sm<sub>0.85</sub>Tm<sub>0.15</sub>S. The incident angle of the laser beam was  $\Theta = 70^\circ$  and the direction of propagation was varied between  $\varphi = 0^\circ$  [100] and  $\varphi = 45^\circ$  [110]. The peaks created by the Stokes and the anti-Stokes scattering process are clearly visible.

single crystal was polished until it became golden (the typical sign of the occurred phase change). This sample was measured in reflection mode again. Two lattice constants were found in the same spectrum, one for the untouched bulk with the same value as before and one for the polished surface, which was about 3.6% smaller than the lattice constant of the bulk material. In Table 6.3 the measured lattice constants are tabulated together with the mass density.

### 6.3.2 Experimental details

As for the La doped SmS, all  $\text{Sm}_{1-x}\text{Tm}_x\text{S}$  sample were hit by the laser beam under an angle of  $70^\circ$ . The free spectral range was set to 15 GHz and the power on the samples was held below 40 mW. All three samples were measured in five different directions ( $\varphi = 0^\circ[100], 10^\circ, 20^\circ, 35^\circ$  and  $45^\circ[110]$ ) to get the whole angular dispersion relation (Fig. 6.10).

Because of the high reflectivity of the samples (for  $\text{Sm}_{0.90}\text{Tm}_{0.10}\text{S}$  and  $\text{Sm}_{0.85}\text{Tm}_{0.15}\text{S}$  due to the gold film, and for  $\text{Sm}_{0.75}\text{Tm}_{0.25}\text{S}$  by itself), only scattering on surface acoustic waves occurs (see section 6.2.2). Fig. 6.9 shows the spectra of  $\text{Sm}_{0.85}\text{Tm}_{0.15}\text{S}$  in all five directions. One spectrum, with the use of 256 channels of the photon counter, needed a sampling time of about 2 hours. Clearly visible are the peaks generated by the Stokes and the anti-Stokes scattering process on SAWs. To avoid reaction with the humidity of the environment, the not protected  $\text{Sm}_{0.75}\text{Tm}_{0.25}\text{S}$  sample was measured in a specially designed, gas proof sample holder, filled with He gas.

### 6.3.3 Calculated elastic constants

For each sample the elastic constants were calculated. For the elastic constants of the  $\text{Sm}_{1-x}\text{Tm}_x\text{S}$  with a protecting gold film the model of a SAW in a thin film (section 2.2.6) was used directly. The elastic constants of the unprotected 25% Tm doped SmS-compound was calculated with the simple model of a SAW in a semi infinite medium (section 2.2.5). As starting values for the Levenberg-Marquard fit algorithm [20] the elastic constants of the similar La doped SmS were applied. For the elastic constants of the gold layer, the values of polycrystalline and isotropic gold was used, as described in detail in section 6.2.3.

Once more  $C_{11}$  and  $C_{12}$  are strongly coupled and compensate each other. To solve this problem we fixed these constants together with the bulk modulus, measured in a

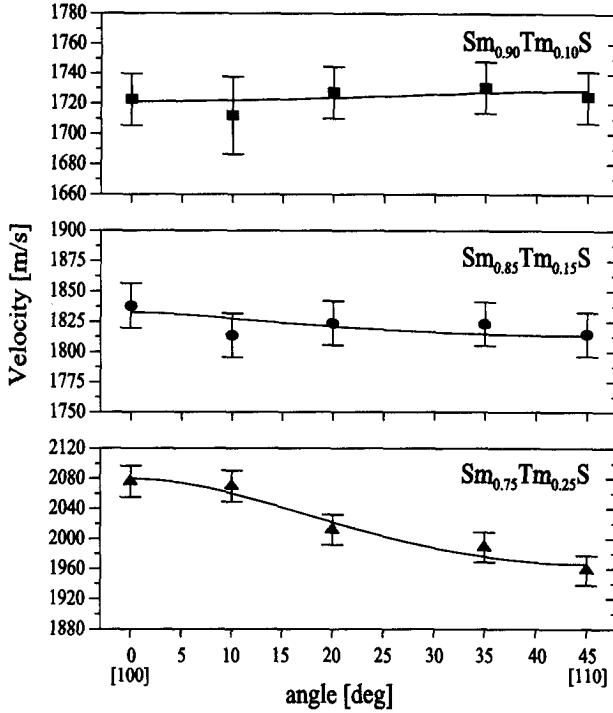


Fig. 6.10 Angular dispersion of the SAW in the (100)-plane of  $\text{Sm}_{1-x}\text{Tm}_x\text{S}$  with  $x = 0.90, 0.85$  and  $0.75$ . The errors are all about 1%. The lines are generated using the elastic constants calculated as described in the text.

volume-pressure experiment by Jung et al. [71]. The accuracy of the fitting process was improved by applying the least square algorithm iteratively.

The calculated elastic constants together with Poisson's ratio and the bulk moduli are tabulated in Table 6.4. The errors are estimated by the error of the measurement and the inaccuracy of the fit. In Fig. 6.11  $C_{11}$ ,  $C_{12}$ ,  $C_{44}$  and the bulk moduli are plotted as a function of the doping concentration. Interesting is the behavior of  $C_{12}$  and, with it, the behavior of Poisson's ratio (Fig. 6.12). At a Tm doping concentration of 10%  $C_{12}$  is clearly positive. This agrees well with the measurements

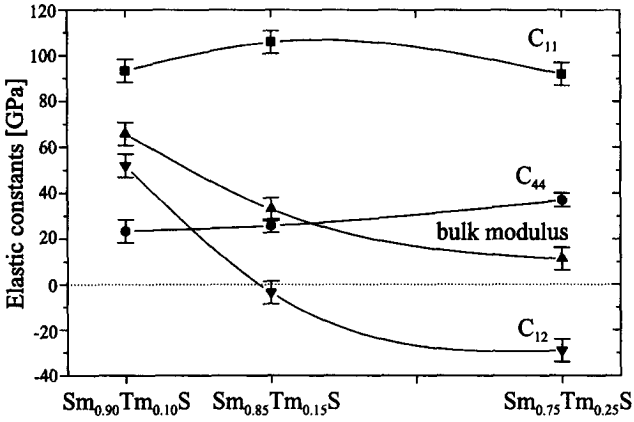


Fig. 6.11 Calculated elastic constants and measured bulk modulus of  $Sm_{1-x}Tm_xS$  versus the doping concentration of Tm

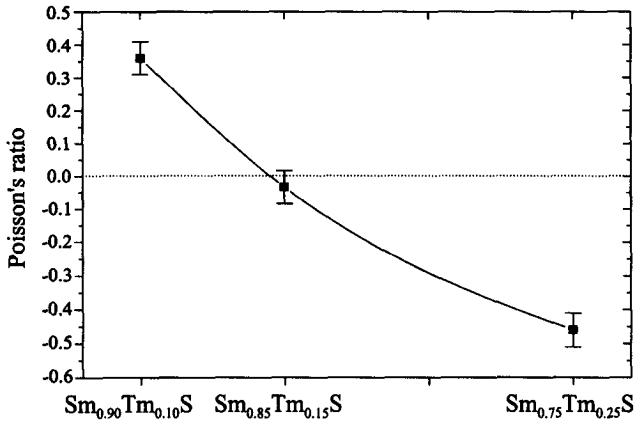


Fig. 6.12 Calculated Poisson's ratios of  $Sm_{1-x}Tm_xS$  as a function of the doping concentration of Tm.

	$C_{11}$ [GPa]	$C_{12}$ [GPa]	$C_{44}$ [GPa]	Bulk modulus $B$ [GPa]	Poisson's ratio $\nu$
$\text{Sm}_{0.90}\text{Tm}_{0.10}\text{S}$	$93 \pm 10$	$52 \pm 10$	$23 \pm 3$	$66 \pm 10$	$0.36 \pm 0.06$
$\text{Sm}_{0.85}\text{Tm}_{0.15}\text{S}$	$106 \pm 10$	$-3 \pm 10$	$26 \pm 3$	$33 \pm 10$	$-0.03 \pm 0.05$
$\text{Sm}_{0.75}\text{Tm}_{0.25}\text{S}$	$92 \pm 10$	$-29 \pm 10$	$37 \pm 3$	$12 \pm 10$	$-0.46 \pm 0.15$

**Table 6.4** The calculated elastic constants, the bulk moduli and the Poisson's ratio of  $\text{Sm}_{1-x}\text{Tm}_x\text{S}$

of the lattice constants and the interpretation by Smirnov et al. [74]:

Both cations, Sm and Tm, are divalent and therefore no intermediate valence can be found. At 15% Tm  $C_{12}$  and Poisson's ratio turn out to be slightly negative and at 25% both are clearly negative. This behavior also fits well to Smirnov's data. In the first case the thulium changes its valence from 2 to 3. Following Smirnov, this change happens quite abruptly, which explains the only slightly negative values of the  $C_{12}$  and Poisson's ratio. In  $\text{Sm}_{0.75}\text{Tm}_{0.25}\text{S}$  already all thulium is trivalent and the intermediate valent behavior comes from the valence change of the samarium, which starts at about 25% Tm in the  $\text{SmS}$  compound. In contrast to the valence change of the Tm, here the change occurs over the whole range from 25% to 100%. This large range may explain the strong negative values of  $C_{12}$  and Poisson's ratio, that we found.

## 6.4 Conclusions

Brillouin spectroscopy experiments have been performed on La and Tm doped single-crystalline  $\text{SmS}$ . The doped compounds were expected to be intermediate valent and therefore to have a negative  $C_{12}$  and negative Poisson's ratio.

Using the measured sound velocities of the surface acoustic waves, the elastic constants and Poisson's ratios of  $\text{Sm}_{1-x}\text{La}_x\text{S}$  ( $x = 0.10, 0.25$  and  $0.35$ ) and of  $\text{Sm}_{1-x}\text{Tm}_x\text{S}$  ( $x = 0.10, 0.15$  and  $0.25$ ) were calculated. All samples, except  $\text{Sm}_{0.90}\text{Tm}_{0.10}\text{S}$ , display a negative  $C_{12}$  and a negative value of Poisson's ratio. While,



at a doping concentration of about 25% La, the  $\text{Sm}_{1-x}\text{La}_x\text{S}$  compounds show a clear minimum of  $C_{12}$  and Poisson's ratio, the  $\text{Sm}_{1-x}\text{Tm}_x\text{S}$  samples have no extrema.

This examination demonstrates once more the strong coupling between the elastic constants and the valence of intermediate valent systems. The behavior of the elastic constants of all samples,  $\text{Sm}_{1-x}\text{La}_x\text{S}$  and  $\text{Sm}_{1-x}\text{Tm}_x\text{S}$ , is in good agreement with the valence of their cations. For integer value of the valence ( $\text{Sm}_{0.90}\text{Tm}_{0.10}\text{S}$ ) no negative  $C_{12}$  and negative Poisson's ratio can be found. Negative values imply always a broken valence of one of the cations. The more negative  $C_{12}$  and the Poisson's ratio are the more broken is the valence. Therefore, the determination of the elastic constants is a powerful way to investigate the intermediate valence.

With the found intermediate valence in the La doped SmS compounds it is clearly demonstrated, that, because of the only minutely smaller ionic radius of the trivalent lanthanum, free electrons in the  $5d$  band play a significant part in making a material intermediate valent. The lattice constants give a further evidence for this Falicov-Kimball-model [62]. The lattice constant of  $\text{Sm}_{0.65}\text{La}_{0.35}\text{S}$  is smaller than the one of pure LaS (Table 6.1 and Fig. 6.7). Therefore the lanthanum can not apply any lattice pressure. Nevertheless  $\text{Sm}_{0.65}\text{La}_{0.35}\text{S}$  is intermediate valent as the negative value of Poisson's ratio proves. Consequently the intermediate valence must be the effect of the induced free electrons of the La-atoms.

# Appendix A

## Further elastic properties

### A.1 Elastic constants of polycrystalline materials

The calculation of the elastic constants of a polycrystalline material ( $C'_{11}$ ,  $C'_{12}$ ,  $C'_{44}$ ) from the elastic constants of its single crystal phase can be done by the use of *Voigt's* average [53]:

$$C'_{11} = C_{11} - \frac{2}{5} \cdot X \quad \text{A.1}$$

$$C'_{12} = C_{12} + \frac{1}{5} \cdot X \quad \text{A.2}$$

$$C'_{44} = C_{44} + \frac{1}{5} \cdot X \quad \text{A.3}$$

with  $X = C_{11} - C_{12} - 2 \cdot C_{44}$  The compliance constants can be transformed in a similar way using *Reuss'* average:

$$S'_{11} = S_{11} - \frac{2}{5} \cdot Y \quad \text{A.4}$$

$$S'_{12} = S_{12} + \frac{1}{5} \cdot Y \quad \text{A.5}$$

$$S'_{44} = S_{44} + \frac{4}{5} \cdot Y \quad \text{A.6}$$

with  $Y = S_{11} - S_{12} - \frac{1}{2} \cdot S_{44}$

## A.2 Lattice constant and Poisson's ratio in films

In a strained layer the lattice constants  $a$  of the relaxed structure can not be measured directly. Instead the lattice constants parallel  $a_{\parallel}$  and perpendicular  $a_{\perp}$  to the surface can be determined. Then, the strains parallel and perpendicular to the surface are given by [50]:

$$\varepsilon_{\parallel} = \frac{a_{\parallel} - a}{a} \quad \text{A.7}$$

$$\varepsilon_{\perp} = \frac{a_{\perp} - a}{a} \quad \text{A.8}$$

Furthermore, a trigonal strain can be defined by:

$$\varepsilon_t = \varepsilon_{\parallel} - \varepsilon_{\perp} = \frac{a_{\parallel} - a_{\perp}}{a} \quad \text{A.9}$$

As described in [52], in a cubic medium the following expression can be found for a (111) oriented surface:

$$\frac{\varepsilon_{\parallel}}{\varepsilon_t} = \frac{C_{11} + \frac{2}{3} \cdot C}{C_{11} + 2 \cdot C_{12}} \quad \text{A.10}$$

Where  $C = 2 \cdot C_{44} - C_{11} + C_{12}$  (Eq. 2.17). For an isotropic material  $C$  vanishes and Eq. A.10 becomes:

$$\frac{\varepsilon_{\parallel}}{\varepsilon_t} = \frac{a_{\parallel} - a}{a_{\parallel} - a_{\perp}} = \frac{C_{11}}{C_{11} + 2 \cdot C_{12}} = \frac{1 - \nu}{1 + \nu} \quad \text{A.11}$$

Where  $\nu$  is the Poisson' ratio as defined in Eq. 2.16. Eq. A.11 can be brought in the form:

$$a_{\parallel} - a_{\perp} = \frac{1 + \nu}{1 - \nu} \cdot (a_{\parallel} - a) \quad \text{A.12}$$

Then, the lattice constant  $a$  and the Poisson's ratio  $\sigma$  can be obtained by plotting the difference of the strained lattice constant ( $a_{\parallel} - a_{\perp}$ ) as function of  $a_{\parallel}$ .

# Appendix B

## Numerical calculations of the SAW velocity

As mentioned in chapter 2, only in a very few cases it is possible to calculate the velocity of a surface acoustic wave directly from the elastic constants and the density of the material. Generally the velocity can only be found numerically by trying different values of  $v_{SAW}$ . Thereby the quality of the found velocity is determined by the boundary conditions (BC). The better the BCs are fulfilled, the better  $v_{SAW}$ . The BCs, which describe a set of linear equations, are fulfilled exactly, when their determinant vanishes. In the following we give a *cook recipe*, how the velocity of a surface acoustic wave in a semi-infinite medium can be found:

- (1) Guess a good value of  $v_{SAW}$  ( $v_{guess}$ ).
- (2) Insert  $v_{guess}$  into the Christoffel equation (Eq. 2.29). The determinant of (Eq. 2.29) defines now a polynomial of 3<sup>rd</sup> degree in  $b^2$  ( $b$  is the damping constant, see also chapter 2). There are now six roots of  $b_i$ , but only the three roots with  $\text{Re}(b_i) \leq 0$  are interesting for a damped wave.
- (3) Construct the solution  $\mathbf{u}_{SAW}$  depending on the damping constants  $b_i$ .

$$\mathbf{u}_{SAW} = \sum_{i=1}^3 A_i \cdot \mathbf{u}(b_i) \quad \text{B.1}$$

Where  $A_i$  are the unknown coefficients and  $\mathbf{u}$  a damped, plane wave, depending on  $b$  as defined in Eq. 2.32.

- (4) Insert the general solution into the boundary conditions (Eq. 2.31). This defines a homogeneous set of linear equations in  $A_i$ .
- (5) To have a non trivial solution of the  $A_i$ , the determinant of the BC matrix has to

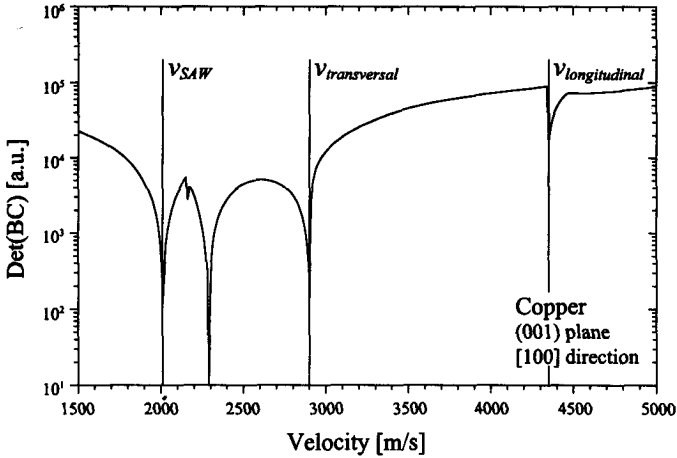


**Fig. B.1** The values of the determinant of the boundary condition matrix versus the velocity in copper along [100] in a (001) plane. The marks denote the velocity of the surface acoustic mode, of the degenerate shear mode and of the longitudinal mode.

vanish. If  $|\det(BC)| = 0$  or, since it is a numerical problem, at least  $|\det(BC)| < \text{const}$ ,  $v_{guess}$  is the velocity of a surface acoustic wave, which fulfills the boundary conditions. If the above condition is not true, a new value for  $v_{SAW}$  has to be found:

$$v_{guess}^{(i+1)} = F(v_{guess}^{(i)}, \det(BC)) \quad \text{B.2}$$

Then go back with the new velocity to (2) and calculate the determinant again.

How fast this iterative process converts depends very much on the method  $F$ , which is chosen to calculate the new value of the velocity. For our calculation we always used the method of Van Wijngaarden, Dekker and Brent (called Brent's method) [20]. In the worst case it converts still linearly to the right solution. To do so, at the start an interval of  $v_{SAW}$  has to be defined in a way, that the right solution lies within the interval.

When the determinant of the boundary condition matrix had only *one* root, that would be enough to find the velocity of a surface acoustic wave. But unfortunately

---

this is not the case. E.g. pure bulk waves can also fulfill the boundary conditions perfectly. Fig. B.1 shows the value of the BC matrix determinant depending on the velocity. Some of the roots have been identified with the wave modes belonging to them. Therefore, every solution, found with the above algorithm, has to be analyzed carefully and rejected, when it is wrong. In [10] conditions for the real Rayleigh like solution are tabulated.

In the case of a wrong solution, it is necessary to change the starting interval in Brent's method to find another solution. For our computer models we have developed an algorithm, that finds the right solution nearly under all circumstances:

- (1) A fixed interval is used. When this fails,
- (2) an interval is calculated from the velocities of the transverse bulk waves. These velocities can always be calculated directly. If this interval still fails,
- (3) the interval is parted in about 100 small intervals and every interval is tried, until one of them returns the right solution. If this method also fails,
- (4) the algorithm capitulates and a senseless value for  $v_{SAW}$  will be returned.

Since we are primarily interested in calculating the elastic constants from the measured SAW velocities, it is necessary to spend so much on creating a stable function. Otherwise it is not possible to use this method as a model function in a fit algorithm like the standard Levenberg-Marquard algorithm.

Leer - Vide - Empty

# References

- [1] B. A. Auld, *Acoustic Fields and Waves in Solids*, I. John Wiley & Sons, Inc. (1973).
- [2] C. Kittel, *Introduction to Solid State Physics*. John Wiley & Sons, Inc., 4<sup>th</sup> edition (1971).
- [3] J. F. Nye, *Physical Properties of Crystals*. Oxford: Clarendon Press (1957).
- [4] R. Vacher and L. Boyer, "Brillouin scattering: A tool for the measurement of elastic and photoelastic constants", *Phys. Rev. B*, **6**, No. 2, 639–673 (1972).
- [5] H. Boppart, A. Treindl, and P. Wachter, "First observation of negative elastic constant in intermediate valent TmSe", *Solid. State. Commun.*, **35**, 483–486 (1980).
- [6] M. Mendik, P. Wachter, J. C. Spirlet, and J. Rebizant, "Intermediate valent PuTe: Negative elastic constants", *Physica B*, **186–188**, 678–680 (1993).
- [7] M. Mendik and P. Wachter, "Brillouin scattering on UTe single crystals", *Physica B*, **190**, 72–73 (1993).
- [8] L. Rayleigh *Proc. London Math. Soc.*, **17**, 4 (1887).
- [9] R. Stoneley, "The propagation of surface elastic waves in a cubic crystal", *Proc. Roy. Soc.*, **232**, 447–458 (1955).
- [10] G. W. Farnell, "Properties of elastic surface waves", in *Physical Acoustics*, **VI** edited by W. P. Mason, Chapter 3, 109–166, New York: Academic Press (1970).
- [11] D. C. Gazis, R. Herman, and R. F. Wallis, "Surface elastic waves in cubic crystals", *Phys. Rev.*, **119**, No. 2, 533–544 (1960).
- [12] M. W. Elmiger, J. Henz, H. von Känel, M. Ospelt, and P. Wachter, "Characterization of crystal surfaces, thin films and superlattices by Brillouin scattering from surface acoustic modes", *Surface and Interface Analysis*, **14**, 18–22 (1989).
- [13] F. R. Rollins, T. C. Lim, and G. W. Farnell, "Ultrasonic reflectivity and surface wave phenomena on surfaces of copper single crystals", *Appl. Phys. Lett.*, **12**, No. 7, 236–238 (1968).
- [14] V. R. Velasco and F. García-Moliner, "Theory of surface waves in anisotropic cubic crystals", *J. Phys. C*, **13**, 2237–2256 (1980).



## References

---

- [15] N. L. Rowell and G. I. Stegeman, "Theory of Brillouin scattering from opaque media", *Phys. Rev. B*, **18**, No. 6, 2598–2615 (1978).
- [16] M. Mendik, S. Sathish, A. Kulik, G. Gremaud, and P. Wachter, "Surface acoustic wave studies on single-crystal nickel using Brillouin scattering and scanning acoustic microscope", *J. Appl. Phys.*, **71**, No. 6, 2830–2834 (1992).
- [17] G. W. Farnell and E. L. Adler, "Elastic wave propagation in thin layers", in *Physical Acoustics*, IX edited by W. P. Mason, Chapter 2, 35–127, New York: Academic Press (1972).
- [18] M. Mendik and P. Wachter, "Brillouin scattering from single-crystal YbX (X=N, P, As)", *Phys. Rev. B*, **47**, No. 10, 6110–6113 (1993).
- [19] E. Sanz-Velasco, O. Hardouin Duparc, and V. R. Velasco, "Acoustic surface waves in cubic crystals with overlayers", *Surf. Sc.*, **126**, 202–207 (1983).
- [20] W. H. Press, B. P. Flannery, T. S. A., and V. W. T., *Numerical Recipes in Pascal, the Art of Scientific Computing*. Cambridge University Press (1986).
- [21] L. Brillouin *Ann. Phys. (Paris)*, **17**, 88 (1922).
- [22] L. I. Mandelstam *Zh. Russ. Fiz. Khim. Ova*, **58**, 281 (1926).
- [23] J. R. Sandercock, "The design and use of a stabilised multipassed interferometer of high contrast ratio", in *Light Scattering in Solids* edited by M. Balkanski, (Paris), 9–12, Flammarion Sciences (1971).
- [24] J. R. Sandercock, "Light scattering from thermally excited surface phonons and magnons", in *7th Int. Conf. On Raman Spectroscopy* edited by F. Murphy, 264–367, North-Holland (1980).
- [25] P. Grünberg, C. M. Mayr, W. Vach, and M. Grimsditch, "Determination of magnetic parameters by means of Brillouin scattering. examples: Fe, Ni,  $\text{Ni}_{0.8}\text{Fe}_{0.2}$ ", *Jour. of Magnetism and Magn. Materials*, **28**, 319–325 (1982).
- [26] G. B. Benedek and K. Fritsch, "Brillouin scattering in cubic crystals", *Phys. Rev.*, **149**, No. 2, 647–662 (1966).
- [27] J. R. Sandercock, "Light scattering from surface acoustic phonons on metals and semiconductors", *Solid State Comm.*, **26**, 547–551 (1978).
- [28] A. M. Marvin, V. Bortolani, and F. Nizzoli, "Surface Brillouin scattering from acoustic phonons: I. general theory", *J. Phys. C*, **13**, 299–317 (1980).
- [29] R. Loudon, "Theory of surface-ripple Brillouin scattering by solids", *Phys. Rev. Lett.*, **40**, No. 9, 581–583 (1978).

- 
- [30] S. Mishra and R. Bray, "Surface-ripple mechanism for Brillouin scattering of reflected light from bulk acoustic waves", *Phys. Rev. Lett.*, **39**, No. 4, 222–225 (1977).
- [31] A. M. Marvin, V. Bortolani, F. Nizzoli, and G. Santoro, "Surface Brillouin scattering from acoustic phonons: II. application to semiconductors", *J. Phys. C*, **13**, 1607–1616 (1980).
- [32] E. Hecht, *Optik*. Addison-Wesley (Deutschland) GmbH (1989).
- [33] M. Hercher, "The spherical mirror Fabry-Pérot interferometer", *Appl. Optics*, **7**, No. 5, 951–966 (1968).
- [34] M. Elmiger, *Raman Scattering under High Pressure in SmSe and Brillouin Spectroscopy from Surface Acoustic Waves*. Diss ETH No. 8692, ETH Zürich (1988).
- [35] R. Loudon, *The Quantum Theory of Light*. Oxford: Clarendon Press, 2<sup>nd</sup> edition (1983).
- [36] B. Houston, R. E. Strakna, and H. S. Belson, "Elastic constants, thermal expansion, and debey temperature of lead telluride", *J. Appl. Phys.*, **39**, 3913–1916 (1968).
- [37] G. Lippmann, O. Kästner, and W. Wanninger, "Elastic constants of PbSe", *Phys. Stat. Sol.*, **6**, No. a, K159–K161 (1971).
- [38] G. I. Peresada, E. G. Ponyatovskii, and Z. D. Sokolovsaya, "Pressure dependence of the elastic constants of PbS", *Phys. Stat. Sol.*, **35**, No. a, K177–K180 (1976).
- [39] C. Maissen, *Epitaktische Bleisalz-Schmalbandhalbleiter auf Siliziumsubstraten*. Diss. ETH Nr. 9930, ETH Zürich (1992).
- [40] P. Müller, *Versetzungen in Strukturierten Bleichalkogenidschichten Auf Silizium*. Diss. ETH Nr. 12011, ETH Zürich (1997).
- [41] J. N. Zemel, J. D. Jensen, and B. Schoolar, Richard, "Electrical and optical properties of epitaxial films of PbS, PbSe, PbTe, and SnTe", *Phys. Rev.*, **140**, No. 1A, A330–A342 (1965).
- [42] W. W. Scanlon *J. Phys. Chem. Solids*, **8**, 423–428 (1959).
- [43] H. von Känel, J. Henz, M. Ospelt, J. Hugi, M. E., and N. Onda, "Epitaxy of metal silicides", *Thin Solid Films*, **184**, 295–308 (1990).
- [44] J. C. Hensel, "Operation of the Si/CoSi<sub>2</sub>/Si heterostrcture transistor", *Appl. Phys. Lett.*, **49**, No. 9, 522–524 (1986).

## References

---

- [45] E. Rosencher, P. A. Badoz, J. C. Pfister, F. Arnaud D'Avitaya, G. Vincent, and S. Delage, "Study of ballistic transport in Si-CoSi<sub>2</sub>-Si metal base transistors", *Appl. Phys. Lett.*, **49**, No. 5, 271–273 (1986).
- [46] C. Schwarz, U. Schärer, P. Sutter, R. Stalder, N. Onda, and H. von Känel, "Application of epitaxial CoSi<sub>2</sub>/Si/CoSi<sub>2</sub> heterostructures to tunable Schottky-barrier detectors", *J. Cryst. Growth*, **127**, 659–662 (1993).
- [47] N. Onda, H. Sirringhaus, S. Goncalves-Conto, C. Schwarz, E. Müller-Gubler, and H. von Känel, "Observation and characterization of the pseudomorphic to stable phase transition of Fe<sub>1-x</sub>Si on Si(111)", *Mat. Res. Soc. Symp. Proc.*, **280**, 581–584 (1993).
- [48] N. Onda, H. Sirringhaus, S. Goncalves-Conto, C. Schwarz, S. Zehnder, and H. Von Känel, "Epitaxy of cubic iron silicides on Si(111)", *Appl. Surf. Science*, **73**, 124–130 (1993).
- [49] S. Goncalves-Conto, *Structural and Electrical Properties of Metallic Epitaxial Silicide Films*. Diss. ETH Nr. 11978, ETH Zürich (1996).
- [50] S. Goncalves-Conto, U. Schärer, E. Müller, and H. von Känel, "A competitive metastable phase in low-temperature epitaxy of CoSi<sub>2</sub>/Si(111)", *Phys. Rev. B*, **55**, 7213 (1997). accepted for publishing.
- [51] H. von Känel, "Growth and characterization of epitaxial Ni and Co silicides", *Mat. Sc. Rep.*, **8**, No. 5, 193–269 (1992).
- [52] J. Hornstra and W. J. Bartels, "Determination of the lattice constant of epitaxial layers of III-V compounds", *J. Cryst. Growth*, **44**, 513–517 (1978).
- [53] M. Mendik, *Brillouin Spectroscopy on Thin Films: Application to Intermediate Valence and Epitaxial Silicides*. Diss. eth no. 10148, ETH Zürich (1993).
- [54] G. Guénin, M. Ignat, and O. Thomas, "Determination of the elastic constants of a cobalt disilicide intermetallic compound", *J. Appl. Phys.*, **68**, No. 12, 6515–6516 (1990).
- [55] L. Weiss, A. Y. Rumamtsev, and A. S. Ivanov *Phys. Stat. Sol.*, **128**, No. b, K111 (1985).
- [56] L. Weber, *Herstellung von CoSi<sub>2</sub>/Fe-Supergittern auf Si(111), strukturelle und elektrische Eigenschaften*. Diploma thesis, ETH Zürich (1996).
- [57] G. Bergmann, "The anomalous Hall effect", *Physics Today*, 25–30 (August 1979).
- [58] P. Wachter and A. Jung, "Intermediate valence and the possibility of a magnetic

- excitonic insulator”, *IEEE Trans. Mag.*, **30**, 954 (1994).
- [59] A. Jayaraman, V. Narayanamurti, E. Bucher, and R. G. Maines, “Pressure-induced metal-semiconductor transition and  $4f$  electron delocalization in  $\text{SmTe}$ ”, *Phys. Rev. Lett.*, **25**, No. 6, 368–370 (1970).
- [60] I. Frankowski and P. Wachter, “Point contact spectroscopy of intermediate valence compounds”, *J Appl. Phys.*, **53**, No. 11, 7887–7889 (1982).
- [61] A. Jayaraman, P. Dernier, and L. D. Longinotti, “Study of the valence transition in  $\text{SmS}$  induced by alloying, temperature, and pressure”, *Phys. Rev. B*, **11**, No. 8, 2783–2794 (1975).
- [62] L. M. Falicov and J. C. Kimball, “Simple model for semiconductor-metal transitions:  $\text{SmB}_6$  and transition-metals oxides”, *Phys. Rev. Lett.*, **22**, No. 19, 997–999 (1969).
- [63] J. M. Robinson, “Valence transitions and intermediate valence states in rare earth and actinide materials”, *Physics Reports*, **51**, No. 1, 1–62 (1979).
- [64] F. Holtzberg, “Effects of lattice pressure in Sm valence states in monosulfide solid solutions”, *AIP Conf. Proc.*, **18**, 478–489 (1974).
- [65] P. Wachter, A. Jung, and P. Steiner, “Pressure-driven metal-insulator transition in La-doped  $\text{SmS}$ : Excitonic condensation”, *Phys. Rev. B*, **51**, No. 8, 5542–5545 (1995).
- [66] J. Neuenschwander and P. Wachter, “Pressure-driven semiconductor-metal transition in intermediate-valence  $\text{TmSe}_{1-x}\text{Te}_x$  and the concept of an excitonic insulator”, *Phys. Rev. B*, **41**, No. 18, 12693–12709 (1990).
- [67] B. Bucher, P. Steiner, and P. Wachter, “Excitonic insulator phase in  $\text{TmSe}_{0.45}\text{Te}_{0.55}$ ”, *Phys. Rev. Lett.*, **67**, No. 19, 2717–2720 (1991).
- [68] P. Wachter. private communications.
- [69] K. Mattenberger, L. Scherrer, and O. Vogt, “Crystal growth of uranium monochalcogenides and monpnictides by mineralization in a special electron beam furnace”, *Jour. Crystal Growth*, **67**, 467–471 (1984).
- [70] E. Zirngiebl and G. Güntherodt in *Light Scattering in Solids*, **VI** edited by M. Cardona and G. Güntherodt, 207 (1991).
- [71] A. Jung and P. Wachter. in preparation.
- [72] *Handbook of Chemistry and Physics*. 57<sup>th</sup> edition. F-213.

## References

---

- [73] I. D. Brown and D. Altermatt, "Bond-valence parameters obtained from a systematic analysis of the inorganic crystal structure database", *Acta Cryst.*, **B41**, 244–247 (1985).
- [74] I. A. Smirnov, V. V. Popov, A. V. Goltsev, A. V. Golubkov, V. A. Shaburov, Y. P. Smirnov, and A. G. Kasymova, "Cascade of phase transition in  $\text{Tm}_{1-x}\text{Sm}_x\text{S}$  due to Tm and Sm valence changes", *J. of Alloys and Compounds*, **219**, 168–171 (1995).
- [75] I. A. Smirnov, A. V. Golubkov, V. M. Sergeeva, E. V. Goncharova, T. B. Zhukova, V. M. Buttaev, M. V. Romanova, N. N. Efremova, and L. D. Finkelstein, "Intermediate valence state of  $\text{Sm}_{1-x}\text{Tm}_x\text{S}$ ", *Physica*, **130B**, 546–547 (1985).

# Publications

C. Schwarz, U. Schärer, P. Sutter, R. Stalder, N. Onda and H. von Känel, "Application of epitaxial  $\text{CoSi}_2/\text{Si}$   $\text{CoSi}_2$  heterostructures to tunable Schottky-barrier detectors", *Journal of Crystal Growth*, Vol **127** (1993), 659-662.

U. Schärer and P. Wachter, "Negative elastic constants in intermediate valent  $\text{Sm}_x\text{La}_{1-x}\text{S}$ ", *Solid State Communications*, Vol **96** (1995), 497-501

U. Schärer and P. Wachter, "Negative elastic constants in intermediate valent  $\text{Sm}_x\text{La}_{1-x}\text{S}$  determined by Brillouin scattering", *Materials Science Forum*, Vols **210-213** (1996), 811-816

U. Schärer and P. Wachter, "Brillouin-spectroscopy on doped  $\text{SmS}$ ", *Conference Proceedings SCES'96* (1996)

U. Schärer and P. Wachter, "Brillouin scattering on intermediate valent  $\text{Sm}_{1-x}\text{La}_x\text{S}$ ", *Europhys Lett.*, Vol **37** (4) (1997), 299-304

S. Goncalves-Conto, U. Schärer, E. Müller, H. von Känel, L. Miglio and F. Tavazza, "A competitive metastable phase in low-temperature epitaxy of  $\text{CoSi}_2/\text{Si}(111)$ ", *Phys. Rev. B*, Vol **55** (1997), 7213

Leer - Vide - Empty

# Presentations

U. Schärer, C. Schwarz und H. von Känel, "Photoelektrische Untersuchungen an epitaktischen  $\text{CoSi}_2/\text{Si}$ -Heterostrukturen, talk, *SPG - Swiss physical Society meeting*, Basle (1992)

U. Schärer und P. Wachter, "neagtives Poisson-Verhältnis von  $\text{Sm}_x\text{La}_{1-x}\text{S}$ ", talk, *SPG - Swiss Physical Society meeting*, Berne (1994)

U. Schärer, "Brillouin-Streuung - Bestimmung der elastischen Konstanten", talk, *ETH Zurich* (1995)

U. Schärer and P. Wachter, "Negative elastic constants in intermediate valent  $\text{Sm}_x\text{La}_{1-x}\text{S}$  measured by Brillouin-spectroscopy", talk, *7<sup>th</sup> International Symposium on Nondestructive Characterization of Materials*, Prague (1995)

U. Schärer, S. Goncalves-Conto, H. vonKänel and P. Wachter, "Brillouin-scattering on thin  $\text{CoSi}_2$ -films", talk, *SPG - Swiss physical Society meeting*, Fribourg (1996)

U. Schärer and P. Wachter, "Brillouin-spectroscopy on doped  $\text{SmS}$ ", poster, *Internatioanl Conference on Strongly Correlated Electron Systems*, Zurich (1996)

U. Schärer, A. Jung and P. Wachter, "Elastic constants in intermedaite valent rare earth compounds determined by Brillouin spectroscopy", invited talk, *Low Energy Electrodynamics in Solids*, Ascona (1997)



Leer - Vide - Empty

# Dank

Am Gelingen dieser Arbeit haben viele Leute ihren Anteil beigetragen, denen ich allen danken möchte. An erster Stelle ist hier Herr Prof. Dr. P. Wachter zu erwähnen, welcher es mir ermöglicht hat, in seiner Forschungsgruppe meine Dissertation auszuführen. Er war immer bereit, mit mir zu diskutieren und mir die Physik, welche hinter seinen Ideen steckt, zu erklären. Sein Enthusiasmus war mir ein Ansporn, und dennoch liess er mir die Freiheit, Eigenes auszuprobieren.

Einen besonderen Dank verdient Herr Prof. Dr. G. Güntherodt, welcher sich bereit erklärt hat, das Korreferat an dieser Arbeit zu übernehmen.

Des weiteren danke ich Herrn PD Dr. H. von Känel und seinen Mitarbeitern, im speziellen Frau Dr. S. Goncalves-Conto und Herrn Dr. C. Schwarz, für die Herstellung und Charakterisierung der  $\text{CoSi}_2$  Schichten und Herrn L. Weber für die Fe/ $\text{CoSi}_2$  Supergitter. Im weiteren gilt mein Dank den Leuten der Sputteranlage, Herrn Dr. A. Weber, Herrn Dr. P. Sutter und Herrn B. Vögeli, für die unzähligen Goldschichten, welche sie mir zwischendurch noch schnell auf einen empfindlichen Kristall gesputtert haben.

Herrn K. Mattenberger danke ich für das Wachsen, Herrn Dr. H. Schwer für die Bestimmung der Gitterkonstanten und Herrn A. Jung für die Messung der Bulk-Moduli der SmS-Verbindungen; Herrn Dr. P. Müller für die Herstellung der PbSe Schichten.

Herrn P. Steiner gilt mein spezieller Dank. Ohne seine Unterstützung und die Einführung in die objektorientierte Programmierung wären die Auswertungsprogramme nicht so elegant und flexibel geworden. Frau Dr. M. Filzmoser, als Nachbarin im gleichen Labor, danke ich für die geduldige Beantwortung all der unzähligen Fragen im Zusammenhang mit der Physik. Herrn PD Dr. L. Degiorgi und Herrn F. Bommeli danke ich für das Korrekturlesen dieser Arbeit und die vielen hilfreichen Diskussionen.

Nicht zu vergessen sind die technischen Mitarbeiter, Herr H. Staub und Herr S. Mollet, welche mir immer mit guten Ratschlägen zur Seite gestanden sind oder für

## Dank

---

mich noch schnell ein Teil an der Drehbank gefertigt haben. Besten Dank!

Nicht unwesentlich zum Gelingen dieser Arbeit beigetragen hat auch das gute und freundschaftliche Arbeitsklima in der Gruppe, was besonders den beiden Sekretärinnen, Frau D. Gini und Frau N. Kubli mit ihrem herzhaften Lachen, aber auch den restlichen Mitarbeitern der Gruppe zu verdanken ist.

# Curriculum Vitae

Name	Urs Schärer
Geboren am	15. Februar 1967 in Winterthur
Bürgerort	Stadt Zürich
1974–1980	Primarschule in Winterthur
1980–1986	Kantonsschule Rychenberg in Winterthur
1986	Eidgenössische Matur Typ B
1986–1987	EDV Praktikum in der Werkzeugmaschinenfabrik Oerlikon-Bührle AG in Zürich
1987–1992	Physik-Studium an der ETH Zürich
1992	Diplom als Physiker der ETH Zürich
1992–1997	Assistent am Laboratorium für Festkörperphysik an der ETH Zürich